Title

Extracellular Matrix Remodeling Regulates Glucose Metabolism through TXNIP Destabilization

Journal

Cell, 175(1)

ISSN

0092-8674

Authors

Sullivan, William J

Mullen, Peter J

Schmid, Ernst W

et al.

Publication Date

2018-09-01

DOI

10.1016/j.cell.2018.08.017

Peer reviewed

Published in final edited form as:

Cell. 2018 September 20; 175(1): 117–132.e21. doi:10.1016/j.cell.2018.08.017.

Extracellular matrix remodeling regulates glucose metabolism through TXNIP destabilization

William J. Sullivan[1,2], **Peter J. Mullen**[1], **Ernst W. Schmid**[1], **Aimee A. Flores**[3,4], **Milica Momcilovic**[5], **Mark S. Sharpley**[3], **David Jelinek**[3], **Andrew E. Whiteley**[1], **Matthew B. Maxwell**[1], **Blake R. Wilde**[6], **Utpal Banerjee**[1,3,4,7], **Hilary A. Coller**[1,3,7,10], **David B. Shackelford**[5,9,10], **Daniel Braas**[2,8], **Donald E. Ayer**[6], **Thomas Q. de Aguiar Vallim**[1,9], **William E. Lowry**[3,4,7,10], and **Heather R. Christofk**[1,2,7,8,10,*]

[1]Department of Biological Chemistry, David Geffen School of Medicine, University of California, Los Angeles (UCLA), Los Angeles, CA 90095, USA

[2]Department of Molecular & Medical Pharmacology, David Geffen School of Medicine, UCLA, Los Angeles, CA 90095, USA

[3]Department of Molecular, Cell, & Developmental Biology, UCLA, Los Angeles, CA 90095, USA

[4]Molecular Biology Institute, UCLA, Los Angeles, CA 90095, USA

[5]Department of Pulmonary & Critical Care Medicine, David Geffen School of Medicine, UCLA, Los Angeles, CA 90095, USA

[6]Department of Oncological Sciences, Huntsman Cancer Institute, University of Utah, Salt Lake City, UT 84112, USA

[7]Eli & Edythe Broad Center of Regenerative Medicine & Stem Cell Research, UCLA, Los Angeles, CA 90095, USA

[8]UCLA Metabolomics Center, Los Angeles, CA 90095, USA

[9]Department of Medicine, David Geffen School of Medicine, UCLA, Los Angeles, CA 90095, USA

[10]Jonsson Comprehensive Cancer Center, UCLA, Los Angeles, CA 90095, USA

SUMMARY

The metabolic state of a cell is influenced by cell-extrinsic factors, including nutrient availability and growth factor signaling. Here, we present extracellular matrix (ECM) remodeling as another

[*]lead contact: hchristofk@mednet.ucla.edu.

Author Contributions

Conceptualization, W.J.S. and H.R.C.; Methodology, W.J.S., P.J.M., M.S.S., D.B., T.Q.V., W.E.L., H.R.C.; Investigation, W.J.S., P.J.M., E.W.S., A.A.F., M.M., M.S.S., D.J., A.E.W., M.B.M., T.Q.V.; Resources, B.R.W. and D.E.A.; Writing – Original Draft, W.J.S. and H.R.C.; Writing - Review & Editing, W.J.S., P.J.M., E.W.S., W.E.L., and H.R.C.; Supervision, U.B., H.A.C., D.B.S., W.E.L., H.R.C.; Funding Acquisition, W.E.L. and H.R.C.

Declaration of Interests

The authors declare no competing interests.

fundamental node of cell-extrinsic metabolic regulation. Unbiased analysis of glycolytic drivers identified the hyaluronan-mediated motility receptor as among the most highly correlated with glycolysis in cancer. Confirming a mechanistic link between the ECM component hyaluronan and metabolism, treatment of cells and xenografts with hyaluronidase triggers a robust increase in glycolysis. This is largely achieved through rapid receptor tyrosine kinase-mediated induction of mRNA decay factor ZFP36, which targets *TXNIP* transcripts for degradation. Since TXNIP promotes internalization of the glucose transporter GLUT1, its acute decline enriches GLUT1 at the plasma membrane. Functionally, induction of glycolysis by hyaluronidase is required for concomitant acceleration of cell migration. This interconnection between ECM remodeling and metabolism is exhibited in dynamic tissue states including tumorigenesis and embryogenesis.

ETOC

The breakdown of extracellular matrix promotes increased tumor cell migration via upregulation of glycolysis.

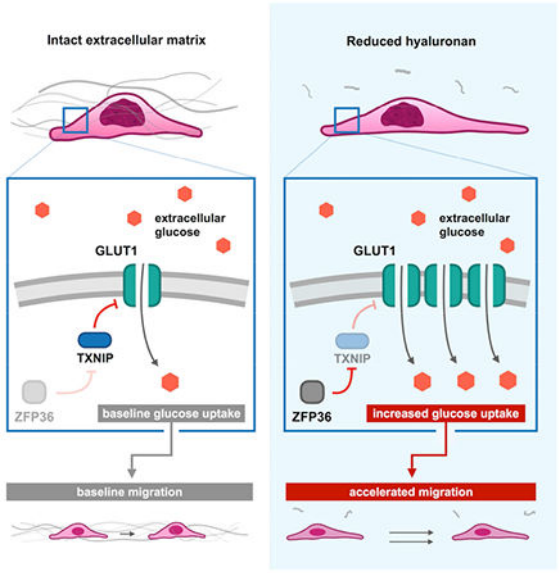

INTRODUCTION

Cells have diverse circuitry to sense and respond to extrinsic metabolic signals. For example, cells coordinate systemic and cellular metabolism by sensing nutrient availability through mTORC1 and shifting between catabolic and anabolic states accordingly (Saxton and Sabatini, 2017); growth factors, hormones, and cytokines can relay metabolic cues to adjacent cells and to distal tissues, as part of a broader biological response. The unifying effect is to integrate the behavior and metabolism of the cell with the requirements of the tissue and organism.

Another cell-extrinsic signal is extracellular matrix (ECM) reorganization, which is central to both tissue expansion and regeneration—with embryogenesis and wound healing being hallmark cases, respectively (Adams and Watt, 1993; Raghow, 1994; Toole, 2001). ECM

remodeling is also a signature of pathological processes, such as tumorigenesis (Bissell and Radisky, 2001; Hanahan and Weinberg, 2011). Many of these processes rely upon increased glycolytic metabolism, which can provision the energetic currency and biosynthetic substrates required for rapid proliferation (DeBerardinis et al., 2008; Purcell and Moley, 2009). Although ECM remodeling and elevated glycolysis are coincident in multiple biological contexts, mechanistic links between these processes are not well established.

Given the importance of anchorage-independent growth to tumorigenesis, categorical changes in matrix attachment and their metabolic implications have been described. ECM detachment of mammary epithelial cells causes a reduction in glucose uptake and subsequent ATP deficiency, both restorable with oncogene expression (Grassian et al., 2011; Schafer et al., 2009). Further supporting the idea that disengagement from the ECM can dramatically alter cell metabolism—specifically by repressing glycolysis—circulating tumor cells show induction of oxidative metabolism compared to their counterparts in both primary tumors and secondary metastatic sites (LeBleu et al., 2014). Collectively, these reports describe the metabolic implications of binary changes in cell attachment to the ECM (i.e., attached vs. detached). What remains unclear is whether specific perturbations in ECM composition can serve as *dynamic* signals to modulate metabolism of cells in the context of a tissue.

Hyaluronan (HA, or hyaluronic acid), a ubiquitous ECM constituent, is a megadalton glycosaminoglycan that ensheaths the cell in a voluminous pericellular matrix through tethering interactions with its plasma membrane (PM) receptors CD44 and the hyaluronan-mediated motility receptor (HMMR)—though interactions with other receptors have been described (Toole, 2001, 2004; Turley et al., 2002). The exact signaling events orchestrated by HA are dependent on its abundance and its size: oligomers of HA have been reported to exert distinct effects on cell behavior (Jiang et al., 2007; Stern et al., 2006). As a result, the biological effects of HA are spatially patterned by the net activity of hyaluronan synthases (the enzymes that synthesize the polymer) and hyaluronidases (the enzymes that cleave it) in proximity of the cell.

Despite the simple structure of the HA polymer—disaccharide repeats of glucuronic acid and GlcNAc—its impacts on both normal biology and pathology are diverse. Beyond regulation of cell behavior through its receptors, HA may have a role in establishing the permissiveness of the environment for cells to proliferate, migrate, and—in cancer—metastasize. Both HA *and* hyaluronidase, however, have been implicated in tumor progression, suggesting either a nonlinear role in the disease or a high degree of subtype specificity (Itano et al., 2002; Toole, 2004; Zhang et al., 1995). The importance of HA in development, however, is clear: deletion of the hyaluronan synthase gene *HAS2* is embryonically lethal given impairment of endothelial cell migration required for cardiac development (Camenisch et al., 2000). In this study, we show that increased migration in response to HA perturbation in cultured cells is dependent on a concomitant increase in glucose metabolism. We show that increased glucose metabolism in response to HA digestion also occurs *in vivo,* and elucidate the signaling mechanisms involved. We therefore propose that ECM remodeling serves as an additional node of acute cell-extrinsic metabolic

regulation, one that can directly read out the structural state of the surrounding tissue and augment cell behavior accordingly.

RESULTS

Unbiased analysis identifies ECM engagement as a regulator of glycolytic metabolism.

We previously described an unbiased analysis to identify genes whose expression correlates with a glycolytic phenotype in breast cancer cell lines and tumors (Hong et al., 2016). Gene expression was correlated with the cellular glycolytic index in 31 breast cancer cell lines, and with uptake of the glucose analog PET tracer ^{18}F-fluorodeoxyglucose (FDG) in 11 patient breast tumors. Genes were rank-ordered based on their average correlation between cell lines and tumors, and *SLC16A1* (encoding monocarboxylate transporter 1, MCT1) had the highest average correlation (Figure 1A). In studies that validate the effectiveness of this unbiased approach—and its potential generalizability beyond breast cancer—we have described the roles that MCT1 plays in cancer cell metabolism and proliferation, and in stem cell pluripotency (Gu et al., 2016).

The second-most correlated gene is the HA receptor *HMMR* (Figure 1A,B). This was surprising as the ECM has not been widely described as a direct regulator of glycolytic metabolism, nor is it often considered in the context of standard cell culture. However, many adherent cell types assemble a pericellular matrix comprised largely of HA polymers anchored to the PM (Cohen et al., 2003). This can be visualized using biotinylated HA binding protein (HABP) (Figure 1C). When cells are treated with bovine testicular hyaluronidase (HAase), the pericellular matrix is digested away, but this does not occur with heat-inactivated HAase (HI HAase).

Consistent with a role for HA in regulating glucose metabolism, LiSa-2 liposarcoma cells treated with HAase for 24h show a dose-dependent induction of glycolysis, as measured by glucose uptake and lactate production (Figures 1D & S1A). HI HAase does not impact glycolysis, suggesting that the effect is mediated by HAase enzymatic activity rather than thermostable contaminants (Figure 1D). Since LiSa-2 cells have a low baseline rate of glucose uptake, we used them—along with additional cell lines—as a model to examine glycolytic activation by HAase.

To confirm that HAase on-target effects are responsible for the induction of glycolysis, LiSa-2 cells were co-treated with HAase and the HAase inhibitor apigenin (Kuppusamy et al., 1990). Apigenin abolishes the effect of HAase on glucose uptake and lactate production (Figure S1B). To further validate that HA modulation culminates in elevated glycolysis, we examined whether chemical inhibition of HA synthesis impacts glucose uptake by treating LiSa-2 cells with 4-methylumbelliferone (4-MU) (Figures 1E & S1C). Disruption of HA pericellular matrix assembly phenocopies HA digestion, with 4-MU increasing glucose consumption (Figure 1F). These data suggest that the absence of full-length HA on the cell surface—by HAase digestion or inhibition of HA synthesis—can trigger an increase in glycolysis.

To determine whether the glycolytic response to matrix digestion with HAase occurs *in vivo,* we examined the effects of HAase in a xenograft model. We imaged A549 xenografts using FDG-PET/CT at baseline and 6h after intratumoral injection with HAase and HI HAase (one preparation per flank, so that each mouse received active and dead enzyme) (Figure 1G). Mean FDG uptake in each HAase-treated tumor was normalized to the paired HI HAase-treated tumor to account for variability among the animals. Tumor FDG uptake increased following HAase treatment, with four out of five mice responding (Figure 1H). These data collectively indicate that matrix digestion with HAase can promote increased glucose metabolism in both cultured cells and tumors.

Matrix digestion with HAase acutely increases glycolytic metabolism in a broad range of cultured cells.

In an attempt to stratify cells that have a glycolytic response to HAase from those that do not, we measured glucose uptake (Figure 2A) and lactate production (Figure 2B) in a panel of cell lines, which included primary and immortalized cells; murine and human cells; as well as cancer cells representing a diversity of genetic lesions. All treated cells show increased glycolytic metabolism. Changes in glutamine uptake (Figure S1D), by contrast, are both bidirectional and of generally smaller magnitude. The differences in glucose and glutamine consumption underscore the specificity of the glycolytic response to HAase.

To assess the timing of the glycolytic response to HAase, we treated cells for 24h and 5d. LiSa-2 cells and mouse embryonic fibroblasts (MEFs) show a sustained response to HAase (Figure 2C). These sustained changes in glycolysis are visually evident in the acidification of the cell culture media, a proxy for lactate production (Figure 2D). 293T cells, however, do not show a similarly sustained response to HAase, with glucose uptake reverting towards the baseline rate after 5d (Figure 2E). This suggests that there may be an acute, universal response to HAase, and a specific, sustained response in certain cell types.

Canonical HA receptors are likely not involved in the glycolytic response to HAase.

We then attempted to determine whether HA interaction with its canonical receptors mediates the glycolytic response to its enzymatic cleavage. HMMR and CD44 are the best characterized, and the latter has been described as a mediator of glycolysis (Slomiany et al., 2009; Tamada et al., 2012). There are, however, divergent changes in levels of these receptors after 24h of HAase treatment (Figure S2A,D).

Consistent with our unbiased analysis suggesting a positive correlation between *HMMR* and glycolysis, HMMR knockdown in LiSa-2 cells causes baseline glucose uptake to fall below the sensitivity of our measurements (Figure S2A,B) despite no effect on cell viability (Figure S2C). HAase treatment, however, lowers HMMR levels (Figure S2A). While the correlation between *HMMR* expression and glycolysis served as a compelling entrée into the study of HA and its impact on metabolism, these results are inconsistent with a direct effect of HMMR levels on the glycolytic response to HAase.

CD44 is upregulated in response to HAase, yet knockdown of the receptor does not abolish the glycolytic response to HAase (Figure S2D,E). While one of the CD44-targeted shRNAs blunts the increase in glucose uptake after HAase treatment, levels of CD44 are not

proportional to glucose uptake. Furthermore, although most cell lines tested show CD44 upregulation after HAase treatment, one shows no change in levels and another does not express CD44 (Figure S2F). While these data suggest that CD44 does not mediate the glycolytic response to HAase, it should be noted that MDA-MB-453 cells, without detectable levels of CD44, show a relatively low magnitude induction of glycolysis (Figure 2A,B). It is therefore possible that *part* of the glycolytic response to HAase is due to binary signaling through CD44 that is irrespective of levels of the receptor.

HAase enriches GLUT1 at the plasma membrane.

To identify the node by which HAase upregulates glycolysis, we examined transcript and protein levels of glycolytic enzymes after HAase treatment and found neither upregulation of the KEGG-defined glycolytic gene set (Figure S2G) nor changes in glycolytic enzyme levels (Figure S2H). We then assessed functional changes, measuring activity of hexokinase (HK), phosphofructokinase (PFK), and lactate dehydrogenase (LDH) (Figure S2I). The only change is a *decrease* in HK activity with treatment. This suggests that there is spare glycolytic capacity at several steps in the pathway and that glucose entry into glycolysis may be rate-limiting.

Analysis of metabolite pool sizes by LC/MS can identify altered nodes in the glycolytic pathway (Hu et al., 2016). If a treatment were to activate a rate-limiting glycolytic enzyme, you would expect to observe a selective increase in downstream metabolites and/or a decrease in its substrate. However, we find that HAase treatment increases levels of all measured glycolytic intermediates in LiSa-2 cells at 6h and 24h, consistent with a bottleneck at the level of glucose availability (Figure 3A). Underscoring the specificity of the glycolytic response, downstream effects of HAase on the TCA cycle are limited: U-$^{13}C_6$-glucose tracer analysis shows increased glucose incorporation into only malate (Figure S2J), coupled with bidirectional changes in intermediate pool sizes (Figure S2K).

To identify whether HAase impacts glucose entry into the cell, we examined subcellular distributions of the canonical glucose transporters, GLUT1–4, following HAase treatment. GLUT1 staining in LiSa-2 cells is concentrated in punctae surrounding the nucleus in control cells, whereas it is more diffuse after HAase treatment (Figure 3B). To confirm that GLUT1 is enriched at the PM, we fractionated cells and see increased GLUT1 (and GLUT3) in the PM fraction after HAase treatment (Figure 3C). Stable MCT1 PM levels indicate that HAase has a specific effect on glucose transporters, rather than promoting global upregulation or redistribution of PM proteins.

We then examined whether changes in PM levels of glucose transporters correspond with changes in glycolysis. We observe both extracellular acidification (ECAR, a real-time proxy for lactate production) and PM GLUT1 and GLUT3 levels are increased by 6h (Figure 3D,E). To further characterize these kinetics, we measured incorporation of U-$^{13}C_6$-glucose carbons into glycolytic intermediates over a time course in HAase-treated MEFs (Figure S2L). Early pathway intermediates (e.g., FBP) are nearly fully labeled at 5min, but DHAP and lactate show escalating incorporation of the tracer over time that is accelerated by HAase. This corresponds with increased pool sizes of glycolytic intermediates after 6h and 24h of treatment (Figure S2M). These data indicate HAase promotes increased glycolysis

starting at 6h, which aligns with the timing of the response in both ECAR and GLUT1 PM localization in LiSa-2 cells (Figure 3D,E).

To determine how HAase regulates GLUT1 and GLUT3, we examined their transcript levels after HAase treatment (Figure 3F). While *SLC2A3* (GLUT3) is upregulated at both time points, *SLC2A1* (GLUT1) is decreased at 4h and upregulated at 24h. Given the inconsistent result with *SLC2A1,* we then measured total protein levels at multiple time points of HAase treatment and in multiple cell lines; GLUT1 levels remain unchanged (Figure 3G). These data suggest that while the increases in PM GLUT3 may be due to transcriptional induction, enrichment of GLUT1 is largely due to changes in subcellular distribution.

To assess whether increases in PM GLUT1 and GLUT3 are universal responses to HAase, we fractionated 293T and MDA-686 cells after HAase treatment (Figure 3H). Both cell lines show increased PM GLUT1 in response to HAase, but do not show similar consistency in GLUT3. We therefore concluded that GLUT1 is likely the common mediator of the glycolytic response to HAase, though changes in transcription or trafficking of other glucose transporters might augment the effect of HAase in some cells.

TXNIP reduction can mediate the acute glycolytic response to HAase.

We then sought to determine how HAase affects GLUT1 localization. There are well established mediators of GLUT1 distribution between intracellular compartments and the cell surface, including TXNIP, whose transcript levels are anti-correlated with a glycolytic phenotype in our initial unbiased analysis (Figure 1A). TXNIP regulates both the transcription and trafficking of GLUT1, the latter by binding PM GLUT1 and promoting its internalization in clathrin-coated pits (Patwari et al., 2009; Wu et al., 2013). TXNIP levels drop acutely after HAase treatment in multiple cell lines (Figure 4A). All cell lines tested show reduced TXNIP levels after 2h of HAase treatment, which may explain the increased PM GLUT1 levels after 6h. To confirm that the TXNIP reduction represents an on-target effect of HAase, we tested two additional enzyme sources: hyaluronidase isolated from *Streptomyces hyaluronlyticus,* and recombinant human PH-20. Both hyaluronidases reduce TXNIP levels with magnitude similar to bovine testicular HAase (Figure S3A).

We next used Txnip knockout (KO) MEFs to test whether the glycolytic response to HAase could be attributed to negative regulation of Glut1 by Txnip. As previously described, Txnip KO cells have higher baseline rates of glucose uptake and lactate production than their WT counterparts (Figure 4B), and have higher baseline PM Glut1 levels (Figure 4C) (Elgort et al., 2010). After confirming that HAase reduces Txnip levels in WT MEFs (Figure 4D), we fractionated both WT and KO MEFs after HAase treatment (Figure 4E). While WT MEFs show a robust induction of PM Glut1, KO cells show only a modest response (Figure 4E heatmap). Consistent with the hypothesis that altered Glut1 trafficking is largely responsible for mediating the glycolytic response to HAase, Txnip KO MEFs show a lower magnitude increase in glucose uptake and lactate production in response to HAase (Figure 4F).

ZFP36 is rapidly induced by HAase and targets *TXNIP* transcripts for degradation.

We next asked what upstream events might culminate in the acute TXNIP reduction following HAase treatment. TXNIP is regulated at both the transcriptional and post-

translational level; the acute change in TXNIP protein suggests the latter possibility. AMPK, a well characterized regulator of glucose metabolism and cellular energy homeostasis, can phosphorylate TXNIP and accelerate its proteasomal degradation (Wu et al., 2013), which we confirmed in LiSa-2 cells using an AMPK activator, A-769662. However, AMPK is not activated in response to HAase treatment (Figure S3B). We then investigated whether JNK pathway activation results in TXNIP depletion. The E3 ubiquitin ligase ITCH targets TXNIP and is activated by JNK phosphorylation—and by HAase (Figure S3C) (Wu et al., 2013; Zhang et al., 2010). Pretreating LiSa-2 cells with a JNK inhibitor, SP600125, prevents ITCH activation upon HAase treatment, but only has a modest rescue effect on TXNIP levels (Figure S3C) and does not result in a decreased induction of glucose uptake (Figure S3D) or GLUT1 PM enrichment (Figure S3E).

To more broadly examine whether HAase treatment results in TXNIP protein degradation, we overexpressed the coding sequence of TXNIP in LiSa-2 cells then treated the cells with HAase. We see a robust decrease in endogenous TXNIP but not in the ectopically expressed TXNIP (Figure 5A). This suggests that the HAase-mediated drop in TXNIP levels is unlikely due to proteasomal degradation and instead likely due to transcriptional repression or mRNA processing of *TXNIP.* Indeed, *TXNIP* transcript levels drop by over 50% after 1h of HAase treatment in 293T, MDA-686, and LiSa-2 cells (Figure 5B).

As there is an AU-rich element (ARE) in the *TXNIP* 3’ untranslated region (UTR), we explored the involvement of mRNA processing. We constructed a reporter with a luciferase gene fused to the *TXNIP* 3’ UTR and measured luminescence in HAase-treated HEK293 cells. Luciferase activity is reduced in treated cells (Figure 5C), indicating HAase either activates mRNA processing factors or targets them towards the *TXNIP* 3’ UTR, both of which would culminate in degradation of the reporter. These results are consistent with matrix digestion by HAase acutely stimulating *TXNIP* mRNA degradation.

We identified an mRNA processing factor whose expression is rapidly induced by HAase in all cell lines tested: zinc finger protein 36 (ZFP36, also known as tristetraprolin) (Figure 5D). Originally cloned and identified as a gene inducible by insulin and TPA, ZFP36 can be rapidly and transiently induced by a variety of mitogens (Blackshear, 2002; Lim et al., 1989), and engages with the AREs of its short-lived target transcripts to promote their destabilization through recruitment of a deadenylase complex (Sandler et al., 2011). Demonstrating that ZFP36 is at least among the processing factors that target the *TXNIP* 3’ UTR, we see a dose-dependent decrease in luciferase activity when a ZFP36 expression vector is co-transfected with the *TXNIP* 3’ UTR reporter, with dose defined as the amount of ZFP36 expression vector DNA transfected (Figure 5E).

To determine whether ZFP36 promotes degradation of *TXNIP* mRNA in response to matrix digestion with HAase, we compared the timing of changes in ZFP36 and TXNIP protein levels (Figure 5F). There is synchronized divergence of the two proteins, with ZFP36 induction preceding the drop in TXNIP in 293T, LiSa-2, and MDA-686 cells. To directly interrogate involvement of ZFP36, we knocked it down in LiSa-2 cells and then treated with HAase (Figure 5G). Both shRNAs reduce ZFP36 induction upon HAase treatment, and the shRNA with the stronger knockdown (shZFP36–2) also shows stronger rescue of TXNIP

levels. Importantly, ZFP36 knockdown in LiSa-2 cells also blocks the increase in glucose uptake upon HAase treatment (Figure 5H). This suggests that ZFP36-mediated degradation of *TXNIP* mRNA plays a critical role in the glycolytic response to HAase in LiSa-2 cells.

To examine whether ZFP36-mediated TXNIP depletion is a common response to HAase treatment, we knocked down ZFP36 in an additional cell line, MDA-686. Strong ZFP36 knockdown with shZFP36–1 rescues the HAase-mediated drop in TXNIP levels (Figure S4A). However, shZFP36–2 causes a weaker knockdown of ZFP36 and shows no rescue of TXNIP protein levels upon HAase treatment. These data suggest that MDA-686 cells may be sensitive to changes in ZFP36. Alternatively, other ZFP36 family members may be important in mediating TXNIP depletion in MDA-686 cells since these cells show upregulation of *ZFP36L1* and *ZFP36L2* in response to HAase, whereas 293T and LiSa-2 cells do not (Figure S4B,C). These ZFP36 family members may collectively target the *TXNIP* transcript for degradation.

TXNIP mRNA is regulated at the transcriptional and post-transcriptional level, and both processes may occur in response to HAase, with their relative importance weighted differently in each cell line. Consistent with its role in programming glycolytic metabolism, MYC can suppress *TXNIP* transcription (Shen et al., 2015). We detect elevated MYC levels in response to HAase in LiSa-2 and MDA-686 cells that coincide with a reduction in TXNIP (Figure 5F). Though expression of ZFP36 and MYC is somewhat synchronous, their effects are likely staggered: ZFP36 acutely targets existing transcripts, whereas MYC tunes transcription in a more protracted way. The speed with which *TXNIP* transcript levels plummet after HAase treatment—coupled with the rescue effect of ZFP36 knockdown—suggests a limited role for MYC in the *acute* regulation of TXNIP. Furthermore, knockdown of MYC in LiSa-2 cells does not affect TXNIP or ZFP36 levels at baseline, nor after 4h of HAase treatment (Figure S4D).

ZFP36 induction in response to HAase is transient (Figure 5F), therefore MYC may be involved in determining which cells have a sustained glycolytic response to HAase—and which do not. LiSa-2 cells have stably elevated MYC levels and enrichment of MYC target transcripts following HAase treatment (Figure S4E), and show higher rates of glucose uptake and lactate production after 5d of HAase treatment compared to 24h (Figure 2C). By contrast, induction of MYC is subtler in 293T cells, and MYC decreases at later time points, corresponding with TXNIP levels returning to baseline after 24h of HAase treatment (Figure 5f). Consistent with MYC being involved in the protracted glycolytic response to HAase, glucose uptake in 293T cells reverts towards baseline after 5d of treatment (Figure 2E).

ZFP36 induction and TXNIP depletion are downstream of HAase-stimulated RTK activation.

To determine whether HAase elicits canonical induction of *ZFP36* through growth factor signaling pathways, we assessed receptor tyrosine kinase (RTK) phosphorylation. After 30min of HAase treatment, PDGFR-β is activated in LiSa-2 cells (Figure S4F) and EGFR in MDA-686 cells (Figure S4G). Ephrin A4 is also phosphorylated in LiSa-2 cells, and ALK and Ephrin B3 in MEFs (Figure S4F,H). To examine whether RTK signaling is upstream of ZFP36 induction, we used MDA-686 cells as they show only EGFR activation in our array, reducing the possibility of redundant signaling events triggered by HAase. We pretreated

cells with the EGFR inhibitor erlotinib at a range of concentrations before adding HAase. Erlotinib suppresses baseline ZFP36 levels and increases TXNIP levels (Figure 5I). When co-treated with HAase, erlotinib blocks ZFP36 induction and the subsequent decrease in TXNIP in a dose-dependent fashion. Whether the effects of HAase are MEK-dependent, however, varies among cell lines. Pretreatment with a MEK inhibitor, PD 325901, results in smaller changes in ZFP36 and TXNIP upon addition of HAase in MDA-686 cells than in LiSa-2 cells and MEFs (Figure S4I). This disparity may result from the diversity of RTKs that can be activated by HAase and the variance in resulting signals from one cell line to another.

To assess whether ZFP36 induction and subsequent *TXNIP* degradation are novel features of growth factor signaling, we stimulated MDA-686 cells with EGF and found that it phenocopies HAase (Figure S4J). These results demonstrate that the metabolic effects of HAase hinge on activation of canonical RTK signaling (schematic in Figure 5J). Furthermore, they suggest a convergence of cell-extrinsic cues—growth factor signaling and matrix remodeling—on a novel mechanism by which the cell can acutely modulate its glucose consumption.

Matrix digestion with HAase accelerates cell migration in a TXNIP- and glucose-dependent fashion.

After establishing the mechanism by which ECM remodeling with HAase impacts glycolytic metabolism, we examined the functional consequences of this increased glucose metabolism, and the biological contexts in which they occur. The ECM is described to exert both mitogenic and migratory effects on cells (Toole, 2001), so we hypothesized that acute metabolic regulation in response to HAase may influence cell proliferation or migration by provisioning biosynthetic intermediates and a rapid pool of ATP.

To examine a potential relationship between proliferation and levels of ECM deposition, we performed immunohistochemical staining of tissue from a murine model of cutaneous squamous cell carcinoma (Figure S5A,B). The tumor-adjacent hyperplastic epidermis shows discrete regions of proliferation—indicated by positive staining for Ki-67—that anti-correlate with strong staining of ECM constituents collagen IV (Figure S5A) and HA (probed with HABP) (Figure S5B). This presents two possibilities: ECM digestion is a secondary effect of proliferation—that once cells respond to proliferative stimuli, they secrete matrix-digesting enzymes to accommodate tissue expansion; or, ECM-digesting enzymes can be secreted by neighboring cells, with changes in the surrounding matrix serving as paracrine proliferative signals.

To test whether HAase directly affects proliferation, we measured cell growth from medium density (some cell-cell contacts) to high density (Figure S5C). In HFF-1, LiSa-2, and MEF cells, treatment with HAase has a minimal impact on proliferation during exponential growth, despite dramatically altering cell morphology (Figure S5C). When cell-cell contacts increase, however, HAase confers a proliferative advantage, suggesting that HAase allows the cell to overcome contact inhibition. While PBS-treated HFF-1 cells and MEFs form monolayers at high density, their HAase-treated counterparts intercalate, forming lattices of cell projections (Figure S5C). To examine whether TXNIP is involved, we measured the

growth of HAase-treated WT and Txnip KO MEFs. Despite their blunted glycolytic response to HAase, Txnip KO MEFs respond to HAase similarly to WT MEFs (Figure S5C). These results suggest that matrix remodeling with HAase promotes high-density cell proliferation by reducing contact inhibition, but TXNIP reduction is not involved in MEFs exposed to the abundant nutrients in cell culture media.

To assess whether HAase increases migration—and whether the glycolytic response to HAase *in vitro* in part supports its energetic requirements—we performed wound healing/scratch assays using WT and Txnip KO MEFs. Consistent with our hypothesis, HAase-treated WT MEFs show an increased rate of scratch closure (Figures 6A & S5D). However, there is no difference in migration between PBS- and HAase-treated Txnip KO MEFs, and their rates of scratch closure are not different from HAase-treated WT MEFs. These results suggest that the HAase-mediated increase in migration may depend on TXNIP downregulation, and that the rate of cell migration may track with that of glycolytic metabolism.

To further assess whether TXNIP downregulation is important for the migratory response, we examined the effects of HAase on scratch closure in cancer cells with either TXNIP KO (MDA-MB-231 breast cancer cells) or overexpression (LiSa-2 cells). Consistent with the prior experiment in MEFs, HAase accelerates scratch closure in WT MDA-MB-231 cells, bringing their rate of migration in line with PBS- and HAase-treated TXNIP KO cells, between which there is no difference (Figure 6B,C). To complement this, we overexpressed the *TXNIP* coding sequence, which cannot be degraded by ZFP36, in LiSa-2 cells (Figure 6D). While HAase increases migration in all control cells, it has no effect in cells overexpressing TXNIP (Figure 6E). These data suggest that ECM remodeling with HAase serves as a migratory signal across cell types, and that TXNIP downregulation via its 3' UTR is a central mediator of this effect.

Since TXNIP reduction is necessary for optimal migration, we assessed whether glucose is limiting for migration by measuring scratch closure in LiSa-2 cells cultured with normal levels of glucose (25mM) and in media with glucose dropped out (1mM) (Figure 6F). While HAase increases scratch closure in both conditions, the rate of closure with HAase treatment is higher in 25mM than 1mM glucose. This result is not confounded by differences in baseline migratory rates as there is no difference between the 1mM and 25mM glucose conditions. Coupled with prior results, this suggests that basal glucose influx is limiting for migration and that the effects of TXNIP on glucose consumption likely mediate the migratory response to HAase. The glycolytic response to ECM digestion with HAase may therefore serve to rapidly generate ATP and fuel a broader migratory response to changes in the ECM.

ECM remodeling influences Zfp36-Txnip-Glut1 signaling in tissue.

Cultured cells are a limited system to study ECM perturbation. Although cultured cells assemble a pericellular matrix, the complexity of the ECM is lower than in most tissue. Although we demonstrated that HAase-treated tumors have increased FDG uptake (Figure 1G,H), we sought to confirm the mechanism of the glycolytic response to HAase in tissue. Given the informative gradients of cell behavior in tumor-adjacent hyperplastic epidermis in

Figure S5A-B, we chemically reproduced hyperplasia of the skin using TPA then intradermally injected it with HAase or HI HAase (Figures 7A & S6A). HA deposits in the hyperplastic epidermis at baseline (HI HAase treatment) are largely extinguished by HAase. In this tissue, as in cell culture, depletion of HA with HAase correlates with increased Zfp36, decreased Txnip, and increased Glut1. This strengthens our cell culture findings and extends their relevance to tissue.

To examine relationships between the ECM, Txnip, Zfp36, and glucose transporters in unmanipulated tissue, we stained neoplasms driven by KrasG12D and loss of p53 in hair follicle stem cells (Figures 7B-E & S6B-D). This is an ideal model as high levels of proliferation and tissue disorganization produce architectural reference points. As expected, there is strong correlation between ECM constituents—HABP and collagen IV—and Txnip (Figures 7B & S6C-D). Collagen IV is smaller than the HA polymer, with more discrete cellular interactions, hence its staining pattern has clearer boundaries than HABP. Furthermore, as HABP can bind partially digested HA fragments, faint signal is expected in areas where the ECM is being actively remodeled.

Consistent with our findings and previous reports, Txnip and Glut1 anti-correlate in these neoplasms (Figures 7C & S6B,D). The regions of strongest HABP staining appear to anti-correlate with *cytoplasmic* Zfp36, Ki-67, and Glut3, reinforcing the possibility of a coordinated metabolic and proliferative response to ECM digestion in nutrient-limited tissue (Figure 7D,E). Cytoplasmic Zfp36 is actively engaged in mRNA processing: some mitogenic signals that induce ZFP36 transcription also lead to its trafficking from the nucleus to the cytosol (Blackshear, 2002). While some baseline nuclear Zfp36 signal overlaps with Txnip and the ECM, cytoplasmic Zfp36 primarily overlaps with Ki-67 and Glut3 (Figure 7D,E). This suggests a relationship between the ECM and ZFP36-TXNIP-GLUT1 signaling that may in part regulate the behavior of cells in complex tissues. For example, these results raise the possibility that spatial differences in ECM deposition may contribute to the metabolic and proliferative heterogeneity of cancer cells in a tumor.

HA digestion may influence glucose metabolism in early mammalian embryos.

Mammalian oocytes are surrounded by the cumulus oophorus, a network of cells held together by a matrix of HA. These cells support oocyte maturation by shuttling pyruvate and other metabolites into it through membrane channels (Kidder and Mhawi, 2002). Sperm cells have GPI-anchored HAase that disperses the cumulus, allowing fertilization of the oocyte (Figure S7A; Lin et al., 1994). HA digestion coincides with the genesis of a metabolically independent zygote.

Though preimplantation embryos rely predominantly on pyruvate, they both express GLUT1 and consume glucose (Purcell and Moley, 2009). It is thought that this glucose is used for biosynthesis, via glycogen synthesis and the pentose phosphate pathway (Gardner et al., 2000). It is also reported that glucose metabolism in murine oocytes can be regulated by *Txnip* (Lee et al., 2013), suggesting that dispersal of the HA-rich cumulus may impact glucose metabolism in the early embryo.

To assess the impact of HAase-mediated cumulus dispersal on glucose metabolism in preimplantation murine embryos, we performed RNA-Seq at sequential cell divisions. Consistent with our previous findings, *Zfp36* increases as *Txnip* decreases after dispersal of the cumulus (Figure S7B). Furthermore, glucose transporter transcript RPKM values remain low at these stages of division (Figure S7C), suggesting that their trafficking may be a more important regulator of glucose metabolism than their transcription in the early embryo. This is consistent with a possible stimulation of glucose metabolism in early mammalian embryos by HAase-mediated regulation of ZFP36 and TXNIP.

DISCUSSION

In this study, we posit matrix remodeling might serve—in addition to its other multivariate effects on the biology of the cell—as a node of acute cell-extrinsic metabolic regulation. That TXNIP integrates ECM signals with metabolism adds to its broad repertoire, which includes acute and protracted regulation of glucose uptake. Studies of TXNIP regulation have focused on two regulatory mechanisms: post-translational modification and transcription. Upon insulin stimulation, Akt phosphorylates TXNIP causing it to disengage from GLUT4, untethering the transporter from clathrins and preventing its endocytosis (Waldhart et al., 2017). Akt targets the same residue that is phosphorylated by AMPK to promote proteasomal degradation of TXNIP (Wu et al., 2013). While signaling can converge on TXNIP, the effects of a single signal can be multifaceted.

Transcriptional regulation of *TXNIP* can be dynamic or sustained. When intracellular glucose levels are elevated, MondoA/MIx binds the carbohydrate response element in the *TXNIP* promoter, upregulating transcription as part of a negative feedback loop (Stoltzman et al., 2008). Conversely, MondoA/MIx activity is repressed when cells enter G_1 and require biosynthetic glucose metabolites for anabolism (Elgort et al., 2010). *TXNIP* is also stably downregulated, most notably by MYC, which represses its transcription as part of a broad glycolytic program (Shen et al., 2015).

Although TXNIP can be modulated by a microRNA during programmed cell death (Lerner et al., 2012), regulation of *TXNIP* transcript stability has not been described in the context of metabolism. Here, we provide evidence for acute regulation of *TXNIP* by the mRNA decay factor ZFP36. Targeting *TXNIP* transcript stability gives the cell a nimble way to regulate its glycolytic rate in response to external stimuli, and to coordinate it with punctuated cellular behaviors like migration. ZFP36 regulation of glucose metabolism has not been previously described, but is likely not limited to ECM remodeling. Because ZFP36 can be induced by both growth factors and cytokines, it may be an additional dimension of their impact on glycolytic metabolism. Like ECM signals, growth factors and cytokines often elicit acute cellular responses, and ZFP36-mediated destabilization of *TXNIP* mRNA may provide a rapid way to upregulate glycolysis without augmenting or reprogramming baseline glycolytic machinery: this is a rapid and reversible way to toggle the glycolytic valve.

This mechanistic link between ECM remodeling and glucose metabolism might further explain the heterogeneity of cells within tissues. Changes in the ECM could elicit spatially and temporally circumscribed cellular responses. Hanahan & Weinberg have lamented the

difficulty of assessing proliferative regulation in normal tissue due to the heterogeneous nature of paracrine signaling—as opposed to cancer cells, they argue, which are easier to understand given constitutive activity of these signals (Hanahan and Weinberg, 2011). But tumors, too, show spatial heterogeneity not only in mutational status but also in metabolism and proliferation (Hensley et al., 2016; Meacham and Morrison, 2013). Our data suggest the possibility that within such asynchronous tissue local modulation of the matrix may be a way to elicit acute coordination of these interdependent processes.

STAR METHODS

KEY RESOURCES TABLE

REAGENT or RESOURCE	SOURCE	IDENTIFIER
Antibodies		
p-ACC (Ser79)	Cell Signaling	Cat# 3661
β-actin	Cell Signaling	Cat# 4970
ALDOA	Cell Signaling	Cat# 3188
CD44	Cell Signaling	Cat# 3578
p-c-Jun (Ser63)	Cell Signaling	Cat# 2361
Collagen IV	Abcam	Cat# ab6586
ENO1	Cell Signaling	Cat# 3810
EGFR	Cell Signaling	Cat# 4267
p-EGFR (Tyr1068)	Cell Signaling	Cat# 3777
ELK-1	Cell Signaling	Cat# 9182
p-ELK-1 (Ser383)	Cell Signaling	Cat# 9181
ERK1/2	Cell Signaling	Cat# 4695
p-ERK1/2 (Thr202/Tyr204)	Cell Signaling	Cat# 4370
GAPDH	Invitrogen	Cat# AM4300
GLUT1	Abcam	Cat# ab115730
GLUT3 (*for immunoblots*)	Abcam	Cat# ab191071
GLUT3 (*for IHC*)	Abcam	Cat# ab15311
HK2	Cell Signaling	Cat# 2867
HMMR/CD168	Abcam	Cat# ab108339
ITCH	Cell Signaling	Cat# 12117
p-ITCH (Thr222)	EMD Millipore	Cat# AB10050
Cytokeratin 14 (K14)	Abcam	Cat# ab181595
Ki-67	Abcam	Cat# ab16667
LDHA	Cell Signaling	Cat# 3582
LDHB	Abcam	Cat# ab75167
MCT1	Abcam	Cat# ab85021
MYC	Cell Signaling	Cat# 5605
Na,K-ATPase	Cell Signaling	Cat# 3010
α-tubulin	Sigma	Cat# T6074

REAGENT or RESOURCE	SOURCE	IDENTIFIER
TXNIP (*for immunoblots*)	Cell Signaling	Cat# 14715
TXNIP (*for IHC*)	Abcam	Cat# ab188865
ZFP36/tristetraprolin (*for immunoblots*)	Cell Signaling	Cat# 71632
ZFP36/tristetraprolin (*for IHC*)	LSBio	Cat# LS-B1572
Goat anti-rabbit IgG, Alexa Fluor 488 conjugate	ThermoFisher	Cat# A-11034
Chemicals, Peptides, and Recombinant Proteins		
Hyaluronidase from bovine testes	Sigma	Cat# H3506
Hyaluronidase from *Streptomyces hyaluronlyticus*	EMD Millipore	Cat# 38-956-1100U
Recombinant human hyaluronidase PH-20	Abcam	Cat# ab174000
4-Methylumbelliferone	Sigma	Cat# M1381
Apigenin	Tocris	Cat# 12-271-0
A-769662	Tocris	Cat# 3336
Erlotinib	Cayman	Cat# 10483
PD 0325901	Sigma	Cat# PZ0162
SP600125	Tocris	Cat# 1496
OCT compound	Fisher Scientific	Cat # 23-730-571
Hyaluronic acid binding protein, bovine nasal cartilage, biotinylated	EMD Millipore	Cat# 385911
Streptavidin, Alexa Fluor 555 Conjugate	ThermoFisher	Cat# S32355
Streptavidin, Alexa Fluor 488 Conjugate	ThermoFisher	Cat# S11223
ProLong Gold Antifade Mountant with DAPI	Invitrogen	Cat# P-36931
U-$^{13}C_6$-glucose	Cambridge Isotope Laboratories	Cat# CLM-1396-1
PolyFect Transfection Reagent	Qiagen	Cat# 220002-078
Polybrene	Santa Cruz	Cat# sc-134220
Puromycin	Invivogen	Cat# ant-pr-1
Blasticidin	Invivogen	Cat# ant-bl-1
Lipofectamine 3000	ThermoFisher	Cat# L3000001
KAPA HiFi DNA polymerase	Kapa Biosystems	Cat# KK2101
FuGENE HD	Promega	Cat# E2311
Mitomycin C	Sigma	Cat# M4287
AEC Substrate Chromogen	Dako	Cat# K3464
Critical Commercial Assays		
Plasma Membrane Protein Extraction Kit	Abcam	Cat# ab65400
Proteome Profiler Human Phospho-RTK Array Kit	R&D Systems	Cat# ARY001B
Avidin/Biotin Blocking Kit	Vector Laboratories	Cat# SP-2001
Luciferase Assay System	Promega	Cat# E1500
RNeasy Kit	Qiagen	Cat# 74104
iScript cDNA Synthesis Kit	Bio-Rad	Cat# 170-8891

REAGENT or RESOURCE	SOURCE	IDENTIFIER
KAPA SYBR FAST	Kapa Biosystems	Cat# KK4611
EnVision+ HRP Peroxidase System	Dako	Cat# K4002
VECTASTAIN Elite ABC-HRP Kit	Vector Laboratories	Cat# PK-6100
Quick-RNA Microprep Kit	Zymo	Cat# R1050
Ovation Ultralow System V2	NuGEN	Cat# 0344-32
Hexokinase Colorimetric Assay Kit	BioVision	Cat# K789
Phosphofructokinase Activity Colorimetric Assay Kit	BioVision	Cat# K776
Deposited Data		
Microarray: LiSa-2 cells (conditions: PBS 24h, HAase 6h & 24h)	This paper	GEO: GSE105034
Experimental Models: Cell Lines		
293T (human embryonic kidney)	Steven Bensinger (University of California, Los Angeles)	RRID: CVCL_0063
3T3-L1 (mouse embryonic fibroblast)	Peter Tontonoz (University of California, Los Angeles)	RRID: CVCL_0123
A431 (human epidermoid carcinoma)	Thomas Graeber (University of California, Los Angeles)	RRID: CVCL_0037
A549 (human lung adenocarcinoma)	Steven Dubinett (University of California, Los Angeles)	RRID: CVCL_0023
HCT116 (human colorectal carcinoma)	Cun-Yu Wang (University of California, Los Angeles)	RRID: CVCL_0291
HCT116 (p53 −/−) (human colorectal carcinoma, isogenic p53 null)	Cun-Yu Wang (University of California, Los Angeles)	RRID: CVCL_HD97
HeLa (human cervical adenocarcinoma)	Steven Bensinger (University of California, Los Angeles)	RRID: CVCL_0030
HFF-1 (human foreskin fibroblast)	ATCC	RRID: CVCL_3285
HPSC: HPSC-TAg-TERT (human pancreatic stellate cells)	Rosa Hwang (MD Anderson Cancer Center)	RRID: CVCL_SA59
Hs578T (human breast carcinoma)	Frank McCormick (University of California, San Francisco)	RRID: CVCL_0332
LiSa-2 (human liposarcoma)	Peter Möller (University of Ulm)	RRID: CVCL_M821
LPS2 (human liposarcoma)	Generated from patient-derived xenografts / Hong Wu (University of California, Los Angeles)	RRID: CVCL_IW35
LPS3 (human liposarcoma)	Generated from patient-derived xenografts / Hong Wu (University of California, Los Angeles)	RRID: CVCL_SA56
MCF-10A (human breast epithelial)	Frank McCormick (University of California, San Francisco)	RRID: CVCL_0598
MCF-12A (human breast epithelial)	Frank McCormick (University of California, San Francisco)	RRID: CVCL_3744
MDA-686 (human oropharyngeal squamous cell carcinoma)	William Lowry (University of California, Los Angeles)	RRID: CVCL_6983
MDA-MB-231 (human breast carcinoma)	Donald Ayer (University of Utah)	RRID: CVCL_0062
MDA-MB-453 (human breast carcinoma)	Frank McCormick (University of California, San Francisco)	RRID: CVCL_0418

REAGENT or RESOURCE	SOURCE	IDENTIFIER
MEF (WT) (mouse embryonic fibroblast)	Donald Ayer (University of Utah)	Paired WT control for RRID: CVCL_SA60
MEF (Txnip−/−) (mouse embryonic fibroblast, *Txnip* null)	Donald Ayer (University of Utah)	RRID: CVCL_SA60
MIA-PaCa-2 (human pancreatic carcinoma)	Timothy Donahue (University of California, Los Angeles)	RRID: CVCL_0428
NCI-H1437 (human lung adenocarcinoma)	Steven Dubinett (University of California, Los Angeles)	RRID: CVCL_1472
NCI-H157 (human squamous cell lung carcinoma)	Steven Dubinett (University of California, Los Angeles)	RRID: CVCL_0463
NCI-H1792 (human lung adenocarcinoma)	Steven Dubinett (University of California, Los Angeles)	RRID: CVCL_1495
NCI-H358 (human bronchioloalveolar carcinoma)	Steven Dubinett (University of California, Los Angeles)	RRID: CVCL_1559
NCI-H441 (human lung adenocarcinoma)	Steven Dubinett (University of California, Los Angeles)	RRID: CVCL_1561
NCI-H460 (human large cell lung carcinoma)	Steven Dubinett (University of California, Los Angeles)	RRID: CVCL_0459
NCI-H520 (human squamous cell lung carcinoma)	Steven Dubinett (University of California, Los Angeles)	RRID: CVCL_1566
NCI-H661 (human large cell lung carcinoma)	Steven Dubinett (University of California, Los Angeles)	RRID: CVCL_1577
NHBE (human normal bronchial epithelial cells, primary)	Lonza	Cat# CC-2541
PANC-1 (human pancreatic epithelioid carcinoma)	Timothy Donahue (University of California, Los Angeles)	RRID: CVCL_0480
SNL76/7 (mouse embryonic fibroblast)	ATCC	RRID: CVCL_K227
SUM149PT (human breast carcinoma)	Frank McCormick (University of California, San Francisco)	RRID:CVCL_3422
SUM159PT (human breast carcinoma)	Frank McCormick (University of California, San Francisco)	RRID: CVCL_5423
U-87 (human glioblastoma)	Paul Mischel (University of California, San Diego)	RRID: CVCL_0022
Experimental Models: Organisms/Strains		
Mouse: SCID Beige: C.B-Igh-1b/GbmsTac-Prkdcscid-Lystbg N7	University of California, Los Angeles	RRID: IMSR_TAC:cbscbg
Mouse: *K15CrePR*: B6;SJL-Tg(Krt1-15-cre/PGR)22Cbd	The Jackson Laboratory	RRID: IMSR_JAX:005249
Mouse: *LSL-KrasG12D*: B6.129-Krastm4Tyj/Nci	National Cancer Institute	RRID: IMSR_NCIMR:01XJ6
Mouse: *p53ff*: FVB.129P2-Trp53/Nci	National Cancer Institute	RRID: MGI:3618506
Mouse: C57BL/6J	The Jackson Laboratory	RRID: IMSR_JAX:000664
Oligonucleotides		
qPCR primers (Table S2)	PrimerBank	https://pga.mgh.harvard.edu/primerbank/
Recombinant DNA		
Scramble: MISSION pLKO.1-puro Non-Mammalian shRNA Control	Sigma	SHC002

REAGENT or RESOURCE	SOURCE	IDENTIFIER
shCD44-1: CD44 MISSION shRNA (human, pLKO.1)	Sigma	TRCN0000296191
shCD44-2: CD44 MISSION shRNA (human, pLKO.1)	Sigma	TRCN0000289308
shHMMR-1: HMMR MISSION shRNA (human, pLKO.1)	Sigma	TRCN0000333645
shHMMR-2: HMMR MISSION shRNA (human, pLKO.1)	Sigma	TRCN0000333647
shZFP36-1: ZFP36 MISSION shRNA (human, pLKO.1)	Sigma	TRCN0000005463
shZFP36-2: ZFP36 MISSION shRNA (human, pLKO.1)	Sigma	TRCN0000424764
tet-scramble: pLKO-Tet-On (human)	Linda Penn (University of Toronto)	N/A
tet-shMYC-1: pLKO-Tet-On (human)	Linda Penn (University of Toronto)	N/A
tet-shMYC-2: pLKO-Tet-On (human)	Linda Penn (University of Toronto)	N/A
3xFLAG TXNIP: pLV[Exp]-Bsd-CMV>3xFLAG/hTXNIP[NM_006472.4]	VectorBuilder	N/A
EV (empty vector): pLVX-TetOne-Puro	Donald Ayer (University of Utah)	N/A
tet-TXNIP: pLVX-TetOne-Puro-TXNIP (human)	Donald Ayer (University of Utah)	N/A
VDUP1 CRISPR/Cas9 KO Plasmid (h)	Santa Cruz	Cat# sc-400664
pGL4.10[luc2]	Promega	Cat# E6651
pcDNA3.1(+)	ThermoFisher	Cat# V79020
pcDNA3.1(+)-TXNIP 3' UTR-luc2 (human)	This paper	N/A
MGC ZFP36 cDNA (human)	GE Dharmacon	Cat# MHS6278-202756824
M4-ZFP36 (human)	This paper	N/A
pCMX β-gal	Thomas Vallim (University of California, Los Angeles)	N/A
Software and Algorithms		
Prism 7	GraphPad	https://www.graphpad.com/scientific-software/prism/
AMIDE	Loening et al., 2003	http://amide.sourceforge.net/
ImageJ	NIH	https://imagej.nih.gov/ij/
TraceFinder 3.1	Thermo Scientific	N/A
TopHat v2.0.10	Trapnell et al., 2009	https://ccb.jhu.edu/software/tophat/index.shtml
Cufflinks 2.1.1 / Cuffdiff 2.1.1	Trapnell et al., 2010	http://cole-trapnell-lab.github.io/cufflinks/
Gene Set Enrichment Analysis (GSEA)	Broad Institute	http://software.broadinstitute.org/gsea/index.jsp
Other		
Bioprofile Basic Analyzer	Nova Biomedical	N/A
Z1 Particle Counter	Beckman Coulter	N/A
G8 PET/CT Preclinical Imaging System	PerkinElmer	N/A
XF96 Extracellular Flux Analyzer	Seahorse Bioscience	N/A
HiSeq 2000	Illumina	N/A
Q Exactive	Thermo Scientific	N/A
UltiMate 3000 RSLC UHPLC	Thermo Scientific	N/A

REAGENT or RESOURCE	SOURCE	IDENTIFIER
Luna 3mm NH2 100A column	Phenomenex	N/A
FACSAria	BD	N/A
LightCycler 480	Roche	N/A
Axio Imager.A1 Microscope	Zeiss	N/A
Axio Imager.M1 Microscope	Zeiss	N/A
Axiovert 40 CFL Microscope	Zeiss	N/A
CX43 Biological Microscope	Olympus	N/A
Eclipse 90i Microscope	Nikon	N/A
Vi-CELL XR Cell Viability Analyzer	Beckman Coulter	N/A

CONTACT FOR REAGENT AND RESOURCE SHARING

Further information and requests for resources and reagents should be directed to and will be fulfilled by the Lead Contact, Heather Christofk (hchristofk@mednet.ucla.edu)

EXPERIMENTAL MODEL DETAILS

Cell culture—Cells were maintained using standard tissue culture procedures in a humidified incubator at 37°C with 5% CO_2 and atmospheric oxygen. 293T (human, female), 3T3-L1 (mouse, male), A431 (human, female), HCT116 WT and p53−/− (human, male), HeLa (human, female), HFF-1 (human, male), HPSC (human, female), Hs578T (human, female), LPS2 (human, male), LPS3 (human, male), MDA-686 (human, male), MDA-MB-231 (human, female), MDA-MB-453 (human, female), WT and Txnip knockout MEFs (mouse, sex unspecified), MIA-PaCa-2 (human, male), PANC-1 (human, male), SNL76/7 (mouse, mixed sex), and U-87 (human, male) cells were cultured in DMEM supplemented with 10% fetal bovine serum (FBS) and 1% penicillin/streptomycin (pen/strep); A549 (human, male), NCI-H1437 (human, male), NCI-H157 (human, male), NCI-H1792 (human, male), NCI-H358 (human, male), NCI-H441 (human, male), NCI-H460 (human, male), NCI-H520 (human, male), and NCI-H661 (human, male) cells in RPMI 1640 supplemented with 10% FBS and 1% pen/strep; LPS3 (human, male) cells in DMEM/F12 supplemented with 10% FBS and 1% pen/strep; LiSa-2 (human, male) cells in DMEM/F12 supplemented with 10% bovine serum and 1% pen/strep; MCF-10A (human, female) and MCF12A (human female) cells in DMEM/F12 supplemented with 5% horse serum, 10μg/mL insulin, 10μg/mL cholera toxin (Sigma), 500ng/mL hydrocortisone, and 20ng/mL EGF; and SUM149PT (human, female) and SUM159PT (human, female) cells in Ham's F12 supplemented with 5% FBS, 1% pen/strep, 5μg/mL insulin, 1μg/mL hydrocortisone, and 10ng/mL EGF. Base media, sera, mitogens, and pen/strep were all obtained from Gibco. NBHE (human, male) cells were grown in proprietary serum-free growth media without antibiotics (Lonza).

LiSa-2 liposarcoma cells were generated and provided by Dr. Peter Möller (University of Ulm), and are a compelling model to study glycolytic activation as they have the lowest baseline glucose uptake rate of any cell line we have tested. All experiments reported here have been performed with these cells unless otherwise indicated.

Additional cell lines tested were purchased or procured from a variety of sources. Liposarcoma cell lines LPS2 and LPS3 were established in our lab from patient-derived xenografts in collaboration with Dr. Hong Wu (University of California, Los Angeles). Immortalized human pancreatic stellate cells (HPSCs) were provided by Dr. Rosa Hwang (MD Anderson Cancer Center) (Hwang et al., 2008), Txnip knockout MEFs and MDA-MB-231 cells by Dr. Donald Ayer (University of Utah), and U-87 cells by Dr. Paul Mischel (University of California, San Diego). All breast lines were gifts from Dr. Frank McCormick (University of California, San Francisco). The following cells were obtained from University of California, Los Angeles, investigators: the lung cancer cell lines from the NCI series and A549 cells from Dr. Steven Dubinett, 293T and HeLa cells from Dr. Steven Bensinger, 3T3-L1 cells from Dr. Peter Tontonoz, A431 cells from Dr. Thomas Graeber, HCT116 cells (both WT and $p53^{-/-}$) from Dr. Cun-Yu Wang, MIA-PaCa-2 and PANC-1 cells from Dr. Timothy Donahue, MDA-686 cells from Dr. William Lowry. HFF-1 and SNL76/6 cells were purchased from ATCC, and NHBE cells from Lonza.

Animal models—All animals were maintained in accordance with standards established by the Institutional Animal Care and Use Committee and the Animal Research Committee at the University of California, Los Angeles.

Xenograft model & FDG-PET imaging.: White SCID (Beige) mice (8wk old females) were acquired from the Department of Radiation Oncology, Division of Molecular and Cellular Oncology Animal Core at the University of California, Los Angeles. Mice were injected subcutaneously in two lower flanks with 5×10^6 A549 cells suspended in 50% PBS / 50% Matrigel. *In vivo* small animal imaging was conducted at the Crump Institute, Preclinical Imaging Technology Center. When tumors were ~200 mm^3 mice were injected via lateral tail vein with ~70-80 μCi 18F-FDG, underwent 60min uptake under 1.5% isoflurane anesthesia, followed by microPET and microCT (G8 PET/CT, PerkinElmer) imaging. The following day, each mouse received intratumoral injection (tumor in one flank) with either active HAase (50μL, 400μg/mL) or heat-inactivated HAase (tumor in the other flank) and 6h later mice underwent second 18F-FDG imaging following the same procedure as above. Quantification of 18F-FDG uptake was done using AMIDE software (Loening and Gambhir, 2003) by drawing region of interest (ROI) over tumor and plotting mean uptake values as percent injected dose per gram (% ID/g).

Genetic model of tumorigenesis.: Mice were acquired from The Jackson Laboratory (*K15CrePR*) and from the National Cancer Institute Mouse Models of Human Cancers Consortium repository (*LSL-KrasG12D* and *p53ff*) and *K15CrePR* mice express mifepristone-inducible cre recombinase driven by the promoter of *Krt15,* a member of the keratin family whose expression is pronounced in epithelial stem cells located in the bulge of the hair follicle. *K15CrePR; KrasG12D; p53ff* animals were treated with intraperitoneal injections of mifepristone (10mg/mL dissolved in sunflower seed oil; 2mg per day) for 3–5d before the start of the second adult hair cycle (10wk postnatal). Papillomas followed by bona fide squamous cell carcinomas developed in treated animals 6–10wk after anagen. Tissues were used for immunohistochemistry.

Chemical model of hyperplasia.: C57BL/6J mice (6wk old males) were acquired from The Jackson Laboratory. Mice were shaven and treated topically with 12-O-tetradecanoylphorbol-13-acetate (TPA) twice over the course of a week to induce hyperplasia of the epidermis. TPA was dissolved in 100% ethanol to 5nM; 100μl was used per application. Each mouse then received an intradermal injection of HAase (50μL, 400μg/mL) into one dorsal flank and HI HAase into the opposite flank. Skin was harvested 6h later.

METHOD DETAILS

Enzyme & drug treatments—Hyaluronidase (HAase) from bovine testes (Sigma) was reconstituted in PBS at 40mg/mL and treated at 1:100 for a final concentration of 400μg/mL. This concentration of HAase was determined based on the dose-response relationship established in LiSa-2 cells (Figure S1A). This concentration is above the minimum dose needed to achieve the maximum glycolytic response in these cells, but was selected to buffer against variations in enzymatic activity between lots of HAase and to account for the possibility of decreased sensitivity in other cells. PBS was used as the vehicle control, paired with the longest HAase treatment when multiple time points were assayed. For multi-day time points, media and enzyme were refreshed every other day as appropriate. Heat-inactivated (HI) HAase was prepared by boiling for 15min at 95°C; the resulting preparation was then quickly centrifuged to remove protein aggregates.

The following additional hyaluronidases were used to confirm on-target effects of the primary enzyme preparation: hyaluronidase isolated from *Streptomyces hyaluronlyticus* (EMD Millipore) and recombinant human PH-20 (Abcam). Hyaluronan was also depleted using 4-methylumbelliferone (Sigma), an inhibitor of HA synthesis. For 4-MU experiments, cells were resuspended and plated in media containing the compound (or solvent, DMSO) so that cells were unable to assemble a pericellular matrix of HA. Metabolic measurements and imaging were performed such that the final readout was collected 48h and 24h after plating, respectively.

Apigenin (Tocris), A-769662 (Tocris), erlotinib (Cayman), PD 325901 (Sigma), and SP600125 (Tocris) were dissolved in DMSO. HAase and apigenin (or DMSO) were coincubated in media for 1 h before being added to cells. Erlotinib, PD 325901, and SP600125 were added to cells 1h prior to addition of HAase. Before interrogation of signaling events, cells were serum starved overnight as indicated.

Metabolic rate measurements—Media glucose, glutamine, and lactate concentrations were measured using a Bioprofile Basic Analyzer (Nova Biomedical). Cells were seeded in 6-well plates at densities such that measurements would be made on subconfluent cells. Media was refreshed 24h after seeding cells; media was also added to empty wells as blank controls. After 24h incubation, 1mL media was removed from each sample and the blanks, and metabolite levels were assessed. Cell number was then determined using a Z1 Particle Counter (Beckman Coulter). Rates were calculated by dividing the difference in metabolite levels between samples and blanks by both the measurement interval (24h) and cell number.

Please note we are cautious about making quantitative inferences regarding the absolute magnitude of the fold changes in glucose uptake and lactate production across cell lines and across experiments. Though these are informative metrics for comparisons across *conditions,* cell lines with very low levels of baseline glycolytic activity (like LiSa-2 cells) can appear to respond with dramatically different magnitude between experiments due to small absolute differences in the denominator of the fold-change calculations (which is to say, the rate in the control condition). These differences are both technical (insensitivity of the instrument in measurement of small changes) and biological (e.g., changes in baseline rate due to passage number, serum lot, sensitivity to solvents such as DMSO). In this report, we focus on internal comparisons of magnitude across conditions within individual experiments and cell lines.

Extracellular acidification rate (ECAR) measurement—Real-time measurements of extracellular pH were completed on a Seahorse XF96 Extracellular Flux Analyzer. LiSa-2 cells were seeded in a XF96 microplate at a density of 5,000 cells/well 48h prior to experiment and maintained under standard tissue culture conditions with treatments of HAase as indicated. Cells were then washed twice with assay media (XF Base Medium supplemented with 17mM glucose and 2.5mM glutamine, pH 7.4) and brought to a final volume of 175μL per well. The microplate was placed in a 37°C incubator without CO_2 for 30min prior to loading the plate into the instrument. The extracellular acidification rate was measured over the course of 75min; midpoint measurements are presented.

Immunoblotting—Whole-cell lysates were prepared with RIPA buffer supplemented with phosphatase inhibitors (20mM sodium fluoride and 1mM sodium orthovanadate) and protease inhibitors (aprotinin, leupeptin, pepstatin – all at 4μg/mL). A Plasma Membrane Protein Extraction Kit (Abcam) was used for fractionation of the PM and the cytosol according to manufacturer's protocol, but with additional centrifugation steps to ensure maximal phase separation. Because we observed that boiling caused aggregation of membrane proteins and poor resolution by SDS/PAGE, lysates were denatured at room temperature for 30min following the addition of sample buffer as this prevented the aggregation of membrane proteins.

The following primary antibodies were used: p-ACC Ser79 (Cell Signaling 3661, 1:1,000), β-actin (Cell Signaling 4970, 1:1,000), ALDOA (Cell Signaling 3188, 1:1,000), CD44 (Cell Signaling 3578, 1:1,000), p-c-Jun Ser63 (Cell Signaling 2361, 1:1,000), EGFR (Cell Signaling 4267, 1:1,000), p-EGFR Tyr1068 (Cell Signaling 3777, 1:1,000), ELK-1 (Cell Signaling 9182, 1:1,000), p-ELK-1 Ser383 (Cell Signaling 9181, 1:1,000), ENO1 (Cell Signaling 3810, 1:1,000), ERK1/2 (Cell Signaling 4695, 1:1,000), p-ERK1/2 Thr202/Tyr204 (Cell Signaling 4370, 1:1,000), GAPDH (Invitrogen AM4300, 1:1,000), GLUT1 (Abcam ab115730, 1:1,000 for whole-cell lysates, 1:5,000 for PM fractions), GLUT3 (Abcam ab191071, 1:1,000), HK2 (Cell Signaling 2867, 1:1,000), HMMR/CD168 (Abcam ab108339, 1:1,000), ITCH (Cell Signaling 12117, 1:1,000), p-ITCH Thr222 (EMD Millipore AB10050, 1:500), LDHA (Cell Signaling 3582, 1:1,000), LDHB (Abcam ab75167, 1:500), MCT1 (Abcam ab85021, 1:1,000), MYC (Cell Signaling 5605, 1:1,000), Na,K-ATPase (Cell Signaling 3010, 1:1,000), α-tubulin (Sigma T6074, 1:10,000), TXNIP

(Cell Signaling 14715, 1:1000), ZFP36/tristetraprolin (Cell Signaling 71632, 1:1000). Where shown, bands were quantified using ImageJ (NIH).

Screening for activation (phosphorylation) of receptor tyrosine kinases was performed using the Proteome Profiler Human Phospho-RTK Array Kit (R&D Systems) per manufacturer's protocol. 100-300μg of cell lysate was used from cells treated with PBS or HAase for 30min.

Fluorescence microscopy

Cultured cells.: Cells were seeded at subconfluent densities on acid-washed coverslips. After indicated treatment, cells were fixed in 4% paraformaldehyde for 20min. For GLUT1 staining, cells were permeabilized for 5min in 0.1% Triton X-100 in PBS then blocked in 10% goat serum in PBS for 30min. For HABP staining, cell membranes remained intact and were blocked using an avidin/biotin blocking kit (Vector Laboratories). Cells were probed with a GLUT1 antibody (Abcam ab115730, 1:100) or biotinylated hyaluronan binding protein (HABP, EMD Millipore, 1:100) overnight at 4°C, then incubated with Alexa Fluor 488-conjugated goat anti-rabbit IgG and Alexa Fluor 555-conjugated streptavidin (both ThermoFisher), respectively, at a dilution of 1:500 in blocking buffer for 1h at room temperature. Coverslips were then mounted with ProLong Gold Antifade with DAPI (Invitrogen) and cured overnight before sealing. GLUT1 images were then collected on a Nikon Eclipse 90i Microscope and HABP on a Zeiss Axio Imager.M1 Microscope.

Tissue sections.: Isolated tissues were embedded fresh in OCT compound (Fisher Scientific). The tissue was sectioned with a Leica 3200 Cryostat, and fixed for 5-10min in 4% paraformaldehyde. All sections were blocked in staining buffer containing appropriate control IgG. The following steps were then performed using the same protocol as cultured cells. Sections were probed with the following antibodies: Glut1 (Abcam ab115730; 1:250), Txnip (Abcam ab188865; 1:100), and ZFP36/tristetraprolin (LSBio LS-B1572, 1:200). Sections were also probed using HABP (EMD Millipore, 1:50). Antibodies and HABP were then incubated, respectively, with Alexa Fluor 488-conjugated goat anti-rabbit IgG and Alexa Fluor 488-conjugated streptavidin (both ThermoFisher) at a concentration of 1:500, and mounted using the same Antifade reagent. Images were collected on a Zeiss Axio Imager.A1 Microscope.

Intracellular metabolite extraction and mass spectrometry-based metabolomics—Cells were seeded in 6-well plates such that they were at ~75% confluency at the time of metabolite extraction. Media containing 10mM U-$^{13}C_6$-glucose (Cambridge Isotope Labs) and PBS or HAase was added to cells at indicated time points before extraction. Cells were washed with 150mM ammonium acetate and scraped into 800μL chilled 50% methanol. 10nM norvaline was added to the suspension as an internal standard, followed by 400μL chloroform. After repeated vortexing, the aqueous layer containing metabolites was transferred to a glass vial and dried under vacuum. Metabolites were resuspended in 100μL 70% acetonitrile (ACN) and 5μL of this solution used for the mass spectrometer-based analysis. The analysis was performed on a Q Exactive (Thermo Scientific) in polarity-switching mode with positive voltage 3.0 kV and negative voltage

2.25 kV. The mass spectrometer was coupled to an UltiMate 3000 RSLC (Thermo Scientific) UHPLC system. Mobile phase A was 5mM NH4AcO, pH 9.9, B) was ACN, and the separation achieved on a Luna 3mm NH2 100A (150 × 2.0mm) (Phenomenex) column. The flow was 300μL/min, and the gradient ran from 15% A to 95% A in 18min, followed by an isocratic step for 9min and re-equilibration for 7min. Metabolites were detected and quantified as area under the curve (AUC) based on retention time and accurate mass (≤ 3ppm) using the TraceFinder 3.1 (Thermo Scientific) software. Relative amounts of metabolites between conditions, as well as percentage of labeling, were calculated and corrected for naturally occurring ^{13}C abundance.

Gene knockdown, knockout & overexpression

Knockdown.: Stable knockdown of gene expression was achieved using targeted shRNA sequences in the pLKO.1-puro backbone (Sigma) and inducible knockdown in the pLKO-Tet-On backbone (Wiederschain et al., 2009). A nonspecific scramble sequence was used as a control in both cases. Knockdown was induced with doxycycline at 500ng/mL at time points indicated. shRNA sequences can be found in Table S1.

Overexpression.: Constitutive expression of TXNIP was achieved using a CMV-driven N-terminal 3xFLAG-tagged TXNIP expression vector with a blasticidin-resistance cassette (pLV[Exp]-Bsd-CMV>3xFLAG/hTXNIP[NM_006472.4]) (Cyagen Biosciences). Inducible expression of TXNIP was achieved using the pLVX-TetOne-Puro backbone (Clontech); cells were treated with doxycycline at 500ng/mL at time points indicated. For inducible expression experiments, an empty vector backbone (EV) was used as a control.

Viral transduction.: For both knockdown and overexpression, lentiviral particles were produced by co-transfecting 293T cells with construct of interest along with the *gag/pol, rev,* and *vsvg* packaging plasmids using PolyFect Transfection Reagent (Qiagen). Virus was collected 48h later, filtered through .45μm pores, and added to subconfluent target cells with 4μg/mL polybrene (Santa Cruz) overnight. Transduced cells were allowed to recover in regular growth media for 24h and then were selected with the appropriate resistance marker: 1μg/mL puromycin or 10μg/mL blasticidin (both Invivogen).

CRISPR knockout.: MDA-MB-231 cells were transfected using Lipofectamine 3000 (ThermoFisher) in a 12-well plate with a pool of plasmids encoding GFP, Cas9, and 1 of 3 TXNIP-specific gRNAs (Santa Cruz) in order to generate indels. Cells were trypsinized into a single cell suspension 48h post transfection, sorted by GFP expression using a FACSAria cell sorter (BD), and seeded in 96-well plates at a density of 1 cell per well. After ~3 wks, wells with colonies were expanded and each clonal line was analyzed for *TXNIP* mRNA by qRT-PCR and protein by western blot.

***TXNIP* UTR reporter analysis—**The human *TXNIP* 3' UTR (1.4kb) was amplified from genomic DNA isolated from Hela cells using KAPA HiFi polymerase (Kapa). The human *TXNIP* UTR sequence was cloned upstream of a luciferase gene (luc2 gene, Promega) in a pcDNA3.1(+) backbone. Human *ZFP36* cDNA (GE Dharmacon) was subcloned into an M4 expression vector backbone, where it is driven by a CMV promoter. The luciferase reporter

construct (100ng) was transfected alongside transfection control plasmid (pCMX β-gal, 50ng) (Tarling et al., 2017) and either increasing amounts of the M4-ZFP36 expression plasmid or pcDNA3.1(+) (up to 50ng) per well of a 48-well plate. Transfection was carried out using FuGENE HD (Promega) according to manufacturer's instructions into HEK293 cells plated onto 48-well dishes (n=6 wells/condition). After overnight incubation with the transfection mixture, media was replaced for further 24h before cells were harvested. Cells were then treated for 0.5-6h with HAase-containing media before being harvested. Cell lysates were assayed for luciferase activity using the Luciferase Assay System (Promega) and luciferase activity was normalized to β-gal activity to correct for differences in transfection efficiency. Data are expressed as fold change relative to *TXNIP* UTR luciferase activity with no experimental treatments.

Quantitative Real-Time PCR—Total RNA was isolated using the Qiagen RNeasy Kit and 700ng was used as template for each cDNA synthesis reaction with the iScript Kit (Bio-Rad). Each reaction was then diluted to a total volume of 100μL with ultrapure water. For qPCR, 2μL of the diluted cDNA was combined with 0.5μM primers and KAPA SYBR FAST master mix (Kapa Biosystems) and amplified on a LightCycler 480 (Roche). Relative quantification was then performed using the $\Delta\Delta C_t$ method with *RPLP0* as the reference gene. Primer sequences can be found in Table S2.

Cell proliferation & viability—Cells were seeded in 6-well plates such that triplicate measurements could be made at each indicated time point. Media was refreshed every other day as appropriate. Cells were trypsinized and counted using a Z1 Particle Counter (Beckman Coulter). Phase-contrast images were captured at indicated time points using a Zeiss Axiovert 40 CFL Microscope. Cell viability was determined by trypan blue exclusion using a Vi-CELL XR (Beckman Coulter).

Wound healing/scratch assay—Cells were grown to confluency in 6-well plates and mitotically inactivated with mitomycin C (10μg/mL for MEFs; 5μg/mL for all others) for 2h to rule out the possibility that differences in proliferation could confound the results. Given rapid rate of scratch closure, MEFs (WT and Txnip KO) and MDA-MB-231 cells (WT and TXNIP KO) were subsequently pretreated for 12h with PBS or HAase before a P20 tip was used to make two intersecting scratches in the monolayer of each triplicate well. Given slower absolute rate of closure, LiSa-2 cells (parental, EV & tet-TXNIP) were treated with PBS or HAase in tandem with monolayer disruption. For the TXNIP overexpression experiment, LiSa-2 cells transduced tet-TXNIP or EV control were additionally pretreated with doxycycline (500ng/mL) or vehicle 12h prior to scratch. For the glucose dropout experiment, parental LiSa-2 cells were switched to media with indicated concentration of glucose at the time of treatment. In all cells, numerous washes with media were performed after scratch to remove cell debris. Phase-contrast images were captured for each well using a Zeiss Axiovert 40 CFL Microscope at indicated times following disruption of the monolayer. Absolute area closed at each time point was determined by manual tracing of wound edges and subsequent area quantification in ImageJ.

Immunohistochemistry—Isolated tissues were fixed overnight in 4% formalin and embedded in paraffin. Sections were then de-paraffinized, prepared for histology, and blocked in staining buffer containing appropriate IgG control. Immunohistochemistry was performed with citrate or Tris buffer antigen retrieval with the following antibodies: collagen IV (Abcam ab6586, 1:500), Glut1 (Abcam ab115730; 1:250), Glut3 (Abcam ab15311; 1:50), K14 (Abcam ab181595, 1:1000), Ki-67 (Abcam ab16667; 1:50), Txnip (Abcam ab188865; 1:100), and ZFP36/tristetraprolin (LSBio LS-B1572, 1:200). The EnVision+ HRP Peroxidase System and AEC Substrate Chromogen (both Dako) were used for detection. Biotinylated hyaluronan binding protein (EMD Millipore, 1:50) was also used as a probe, and detected with the VECTASTAIN Elite ABC-HRP Kit (Vector Laboratories). Images were collected on a CX43 Biological Microscope (Olympus).

RNA-Seq library construction & analysis—Total RNA was isolated from murine embryos derived as previously described (Nagaraj et al., 2017) using the Quick-RNA Microprep Kit (Zymo) according to manufacturer's protocol. Total RNA fraction was processed and libraries were generated using the Ovation Ultralow Library System V2 (NuGEN). The resulting purified cDNA library was sequenced on the Illumina HiSeq 2000. 50bp single-end RNA-seq reads were obtained, and sequence files were generated in FASTQ format. The quality score of RNA-seq reads was obtained using FastQC. Reads were then aligned to the UCSC mm10 *Mus musculus* reference sequence from Illumina iGenome using TopHat v2.0.10 (Trapnell et al., 2009). Transcript assembly and estimation of abundance were performed with Cufflinks 2.1.1. Differential expression of genes across conditions was calculated with Cuffdiff 2.1.1 (Trapnell et al., 2010).

Gene Set Enrichment Analysis (GSEA)—Total RNA was isolated with the Qiagen RNeasy Kit and used by the UCLA Clinical Microarray Core to perform whole-genome expression analysis with the GeneChip Human Genome U133 Plus 2.0 array (Affymetrix). Gene set enrichment analysis (Subramanian et al., 2005) was performed using annotations in the Molecular Signatures Database (MSigDB) C2 collection.

Enzymatic activity assays—The Hexokinase Colorimetric Assay Kit and Phosphofructokinase Activity Colorimetric Assay Kit (both BioVision) were used per manufacturer's protocol with 5μg and 0.1 μg cell lysate, respectively. Readout absorbance at 450nm is proportional to NADH production. Lactate dehydrogenase activity was measured by NADH fluorescence (absorption: 340nm, emission: 465nm) when 2μg lysate was combined with 100μL kinetic buffer (50mM Tris pH 7.5, 100mM KCl, 5mM $MgCl_2$, 1mM pyruvate). In all cases, enzyme activity was calibrated against an NADH standard curve.

QUANTIFICATION AND STATISTICAL ANALYSIS

All experiments were performed in biological triplicate unless otherwise indicated. The "N" for each experiment can be found in the figure legends and represents independently generated samples for *in vitro* experiments, cell populations / wells for live cell experiments, and mice for all *in vivo* experiments. Bar graphs present the mean ± SD; p-values were generated for these, and for heatmaps of metabolite pool sizes, by two-tailed Student's t-test. *HMMR* expression scatter plots were analyzed by linear regression. Throughout the figures,

asterisks indicate the significance of the p-value: *p<0.05; **p<0.01; ***p< 0.001. A significant result was defined as p<0.05. Date were analyzed and visualized using GraphPad Prism.

DATA AVAILABILITY

Microarray data have been deposited in NCBI's Gene Expression Omnibus (GEO Series accession GSE105034)

Supplementary Material

Refer to Web version on PubMed Central for supplementary material.

Acknowledgments

We thank Yonggang Zhou for technical assistance in generating RNA-Seq data from murine embryos, and William Tu for designing shMYC sequences. W.J.S. was supported by the UCLA Tumor Cell Biology Training Program (USHHS Ruth L. Kirschstein Institutional National Research Service Award # T32 CA009056). W.E.L. and H.R.C. were supported by R01 AR070245. H.R.C. was also supported by RO1 CA215185, a Research Scholar Grant (RSG-16-111-01-MPC) from the American Cancer Society and the UCLA Jonsson Comprehensive Cancer Center and Eli and Edythe Broad Center for Regenerative Medicine Ablon Scholars Program.

REFERENCES

Adams JC, and Watt FM (1993). Regulation of development and differentiation by the extracellular matrix. Development 117, 1183–1198. [PubMed: 8404525]

Bissell MJ, and Radisky D (2001). Putting tumours in context. Nat Rev Cancer 1, 46–54. [PubMed: 11900251]

Blackshear PJ (2002). Tristetraprolin and other CCCH tandem zinc-finger proteins in the regulation of mRNA turnover. Biochemical Society Transactions 30, 945–952. [PubMed: 12440952]

Camenisch TD, Spicer AP, Brehm-Gibson T, Biesterfeldt J, Augustine ML, Calabro A, Jr., Kubalak S, Klewer SE, and McDonald JA (2000). Disruption of hyaluronan synthase-2 abrogates normal cardiac morphogenesis and hyaluronan-mediated transformation of epithelium to mesenchyme. The Journal of Clinical Investigation 106, 349–360. [PubMed: 10930438]

Cohen M, Klein E, Geiger B, and Addadi L (2003). Organization and Adhesive Properties of the Hyaluronan Pericellular Coat of Chondrocytes and Epithelial Cells. Biophysical Journal 85, 1996–2005. [PubMed: 12944312]

DeBerardinis RJ, Lum JJ, Hatzivassiliou G, and Thompson CB (2008). The Biology of Cancer: Metabolic Reprogramming Fuels Cell Growth and Proliferation. Cell Metabolism 7, 11–20. [PubMed: 18177721]

Elgort MG, O'Shea JM, Jiang Y, and Ayer DE (2010). Transcriptional and Translational Downregulation of Thioredoxin Interacting Protein Is Required for Metabolic Reprogramming during G(1). Genes & Cancer 1, 893–907. [PubMed: 21779470]

Gardner DK, Pool TB, and Lane M (2000). Embryo Nutrition and Energy Metabolism and Its Relationship to Embryo Growth, Differentiation, and Viability. Semin Reprod Med 18, 205–218. [PubMed: 11256170]

Grassian AR, Metallo CM, Coloff JL, Stephanopoulos G, and Brugge JS 2011 Erk regulation of pyruvate dehydrogenase flux through PDK4 modulates cell proliferation. Genes & Development 25, 1716–1733.

Gu W, Gaeta X, Sahakyan A, Chan Alanna B., Hong Candice S., Kim R, Braas D, Plath K, Lowry William E., and Christofk Heather R. (2016). Glycolytic Metabolism Plays a Functional Role in Regulating Human Pluripotent Stem Cell State. Cell Stem Cell 19, 476–490. [PubMed: 27618217]

Hanahan D, and Weinberg Robert A. (2011). Hallmarks of Cancer: The Next Generation. Cell 144, 646–674. [PubMed: 21376230]

Hensley Christopher T., Faubert B, Yuan Q, Lev-Cohain N, Jin E, Kim J, Jiang L, Ko B, Skelton R, Loudat L, et al. (2016). Metabolic Heterogeneity in Human Lung Tumors. Cell 164, 681–694. [PubMed: 26853473]

Hong CS, Graham NA, Gu W, Espindola Camacho C, Mah V, Maresh EL, Alavi M, Bagryanova L, Krotee PAL, Gardner BK, et al. (2016). MCT1 Modulates Cancer Cell Pyruvate Export and Growth of Tumors that Co-express MCT1 and MCT4. Cell Reports 14, 1590–1601. [PubMed: 26876179]

Hu H, Juvekar A, Lyssiotis Costas A, Lien Evan C., Albeck John G., Oh D, Varma G, Hung Yin P., Ullas S, Lauring J, et al. (2016). Phosphoinositide 3-Kinase Regulates Glycolysis through Mobilization of Aldolase from the Actin Cytoskeleton. Cell 164, 433–446. [PubMed: 26824656]

Hwang RF, Moore T, Arumugam T, Ramachandran V, Amos KD, Rivera A, Ji B, Evans DB, and Logsdon CD (2008). Cancer-Associated Stromal Fibroblasts Promote Pancreatic Tumor Progression. Cancer Research 68, 918–926. [PubMed: 18245495]

Itano N, Atsumi F, Sawai T, Yamada Y, Miyaishi O, Senga T, Hamaguchi M, and Kimata K (2002). Abnormal accumulation of hyaluronan matrix diminishes contact inhibition of cell growth and promotes cell migration. Proceedings of the National Academy of Sciences 99, 3609–3614.

Jiang D, Liang J, and Noble PW (2007). Hyaluronan in Tissue Injury and Repair. Annual Review of Cell and Developmental Biology 23, 435–461.

Kidder GM, and Mhawi AA (2002). Gap junctions and ovarian folliculogenesis. Reproduction 123, 613–620. [PubMed: 12006089]

Kuppusamy UR, Khoo HE, and Das NP (1990). Structure-activity studies of flavonoids as inhibitors of hyaluronidase. Biochemical Pharmacology 40, 397–401. [PubMed: 2375774]

LeBleu VS, O'Connell JT, Gonzalez Herrera KN, Wikman H, Pantel K, Haigis Marcia C, de Carvalho FM, Damascena A, Domingos Chinen LT, Rocha RM., et al. (2014). PGC-1α mediates mitochondrial biogenesis and oxidative phosphorylation in cancer cells to promote metastasis. Nature Cell Biology 16, 992. [PubMed: 25241037]

Lee S-Y, Lee H-S, Kim E-Y, Ko J-J, Yoon TK, Lee W-S, and Lee K-A (2013). Thioredoxin-Interacting Protein Regulates Glucose Metabolism and Affects Cytoplasmic Streaming in Mouse Oocytes. PLOS ONE 8, e70708. [PubMed: 23976953]

Lerner Alana G., Upton J-P, Praveen PVK, Ghosh R, Nakagawa Y, Igbaria A, Shen S, Nguyen V, Backes Bradley J, Heiman M, et al. (2012). IRE1α Induces Thioredoxin-Interacting Protein to Activate the NLRP3 Inflammasome and Promote Programmed Cell Death under Irremediable ER Stress. Cell Metabolism 16, 250–264. [PubMed: 22883233]

Lim RW, Varnum BC, O'Brien TG, and Herschman HR (1989). Induction of tumor promotor-inducible genes in murine 3T3 cell lines and tetradecanoyl phorbol acetate-nonproliferative 3T3 variants can occur through protein kinase C-dependent and -independent pathways. Molecular and Cellular Biology 9, 1790–1793. [PubMed: 2471069]

Lin Y, Mahan K, Lathrop WF, Myles DG, and Primakoff P (1994). A hyaluronidase activity of the sperm plasma membrane protein PH-20 enables sperm to penetrate the cumulus cell layer surrounding the egg. The Journal of Cell Biology 125, 1157–1163. [PubMed: 8195297]

Loening AM, and Gambhir SS (2003). AMIDE: A Free Software Tool for Multimodality Medical Image Analysis. Molecular Imaging 2, 131–137. [PubMed: 14649056]

Meacham CE, and Morrison SJ (2013). Tumour heterogeneity and cancer cell plasticity. Nature 501, 328–337. [PubMed: 24048065]

Nagaraj R, Sharpley MS, Chi F, Braas D, Zhou Y, Kim R, Clark AT, and Banerjee U (2017). Nuclear Localization of Mitochondrial TCA Cycle Enzymes as a Critical Step in Mammalian Zygotic Genome Activation. Cell 168, 210–223. [PubMed: 28086092]

Patwari P, Chutkow WA, Cummings K, Verstraeten VLRM, Lammerding J, Schreiter ER, and Lee RT. (2009). Thioredoxin-independent Regulation of Metabolism by the α-Arrestin Proteins. Journal of Biological Chemistry 284, 24996–25003. [PubMed: 19605364]

Purcell SH, and Moley KH (2009). Glucose transporters in gametes and preimplantation embryos. Trends in Endocrinology & Metabolism 20, 483–489. [PubMed: 19811929]

Raghow R (1994). The role of extracellular matrix in postinflammatory wound healing and fibrosis. The FASEB Journal 8, 823–831. [PubMed: 8070631]

Sandler H, Kreth J, Timmers HTM, and Stoecklin G (2011). Not1 mediates recruitment of the deadenylase Caf1 to mRNAs targeted for degradation by tristetraprolin. Nucleic Acids Research 39, 4373–4386. [PubMed: 21278420]

Saxton RA, and Sabatini DM (2017). mTOR Signaling in Growth, Metabolism, and Disease. Cell 168, 960–976. [PubMed: 28283069]

Schafer ZT, Grassian AR, Song L, Jiang Z, Gerhart-Hines Z, Irie HY, Gao S, Puigserver P, and Brugge JS (2009). Antioxidant and oncogene rescue of metabolic defects caused by loss of matrix attachment. Nature 461, 109. [PubMed: 19693011]

Shen L, O'Shea JM, Kaadige MR, Cunha S, Wilde BR, Cohen AL, Welm AL, and Ayer DE (2015). Metabolic reprogramming in triple-negative breast cancer through Myc suppression of TXNIP. Proceedings of the National Academy of Sciences 112, 5425–5430.

Slomiany MG, Grass GD, Robertson AD, Yang XY, Maria BL, Beeson C, and Toole BP (2009). Hyaluronan, CD44, and Emmprin Regulate Lactate Efflux and Membrane Localization of Monocarboxylate Transporters in Human Breast Carcinoma Cells. Cancer Research 69, 1293–1301. [PubMed: 19176383]

Stern R, Asari AA, and Sugahara KN (2006). Hyaluronan fragments: An information-rich system. European Journal of Cell Biology 85, 699–715. [PubMed: 16822580]

Stoltzman CA, Peterson CW, Breen KT, Muoio DM, Billin AN, and Ayer DE (2008). Glucose sensing by MondoA:Mlx complexes: A role for hexokinases and direct regulation of thioredoxin-interacting protein expression. Proceedings of the National Academy of Sciences 105, 6912–6917.

Subramanian A, Tamayo P, Mootha VK, Mukherjee S, Ebert BL, Gillette MA, Paulovich A, Pomeroy SL, Golub TR, Lander ES, et al. (2005). Gene set enrichment analysis: A knowledge-based approach for interpreting genome-wide expression profiles. Proceedings of the National Academy of Sciences 102, 15545–15550.

Tamada M, Nagano O, Tateyama S, Ohmura M, Yae T, Ishimoto T, Sugihara E, Onishi N, Yamamoto T, Yanagawa H, et al. (2012). Modulation of Glucose Metabolism by CD44 Contributes to Antioxidant Status and Drug Resistance in Cancer Cells. Cancer Research 72, 1438–1448. [PubMed: 22293754]

Tarling EJ, Clifford BL, Cheng J, Morand P, Cheng A, Lester E, Sallam T, Turner M, and de Aguiar Vallim TQ (2017). RNA-binding protein ZFP36L1 maintains posttranscriptional regulation of bile acid metabolism. The Journal of Clinical Investigation 127, 3741–3754. [PubMed: 28891815]

Toole BP (2001). Hyaluronan in morphogenesis. Seminars in Cell & Developmental Biology 12, 79–87. [PubMed: 11292373]

Toole BP (2004). Hyaluronan: from extracellular glue to pericellular cue. Nat Rev Cancer 4, 528–539. [PubMed: 15229478]

Trapnell C, Pachter L, and Salzberg SL (2009). TopHat: discovering splice junctions with RNA-Seq. Bioinformatics 25, 1105–1111. [PubMed: 19289445]

Trapnell C, Williams BA, Pertea G, Mortazavi A, Kwan G, van Baren MJ, Salzberg SL, Wold BJ, and Pachter L (2010). Transcript assembly and quantification by RNA-Seq reveals unannotated transcripts and isoform switching during cell differentiation. Nature Biotechnology 28, 511.

Turley EA, Noble PW, and Bourguignon LYW (2002). Signaling Properties of Hyaluronan Receptors. Journal of Biological Chemistry 277, 4589–4592. [PubMed: 11717317]

Waldhart AN, Dykstra H, Peck AS, Boguslawski EA, Madaj ZB, Wen J, Veldkamp K, Hollowell M, Zheng B, Cantley LC, et al. (2017). Phosphorylation of TXNIP by AKT Mediates Acute Influx of Glucose in Response to Insulin. Cell Reports 19, 2005–2013. [PubMed: 28591573]

Wiederschain D, Susan W, Chen L, Loo A, Yang G, Huang A, Chen Y, Caponigro G, Yao Y.-m., Lengauer C, et al. (2009). Single-vector inducible lentiviral RNAi system for oncology target validation. Cell Cycle 8, 498–504. [PubMed: 19177017]

Wu N, Zheng B, Shaywitz A, Dagon Y, Tower C, Bellinger G, Shen C-H, Wen J, Asara J, McGraw Timothy E., et al. (2013). AMPK-Dependent Degradation of TXNIP upon Energy Stress Leads to Enhanced Glucose Uptake via GLUT1. Molecular Cell 49, 1167–1175. [PubMed: 23453806]

Zeller KI, Jegga AG, Aronow BJ, O'Donnell KA, and Dang CV (2003). An integrated database of genes responsive to the Myc oncogenic transcription factor: identification of direct genomic targets. Genome Biology 4, R69. [PubMed: 14519204]

Zhang L, Underhill CB, and Chen L (1995). Hyaluronan on the Surface of Tumor Cells Is Correlated with Metastatic Behavior. Cancer Research 55, 428–433. [PubMed: 7529138]

Zhang P, Wang C, Gao K, Wang D, Mao J, An J, Xu C, Wu D, Yu H, Liu JO, et al. (2010). The Ubiquitin Ligase Itch Regulates Apoptosis by Targeting Thioredoxin-interacting Protein for Ubiquitin-dependent Degradation. Journal of Biological Chemistry 285, 8869–8879. [PubMed: 20068034]

HIGHLIGHTS

- Extracellular matrix remodeling promotes glucose metabolism in cells and tumors
- ZFP36-TXNIP-GLUT1 signaling increases glycolysis in response to hyaluronan digestion
- RTK activation triggers ZFP36 induction and subsequent *TXNIP* mRNA degradation
- The migratory response to hyaluronidase is dependent on glycolytic activation

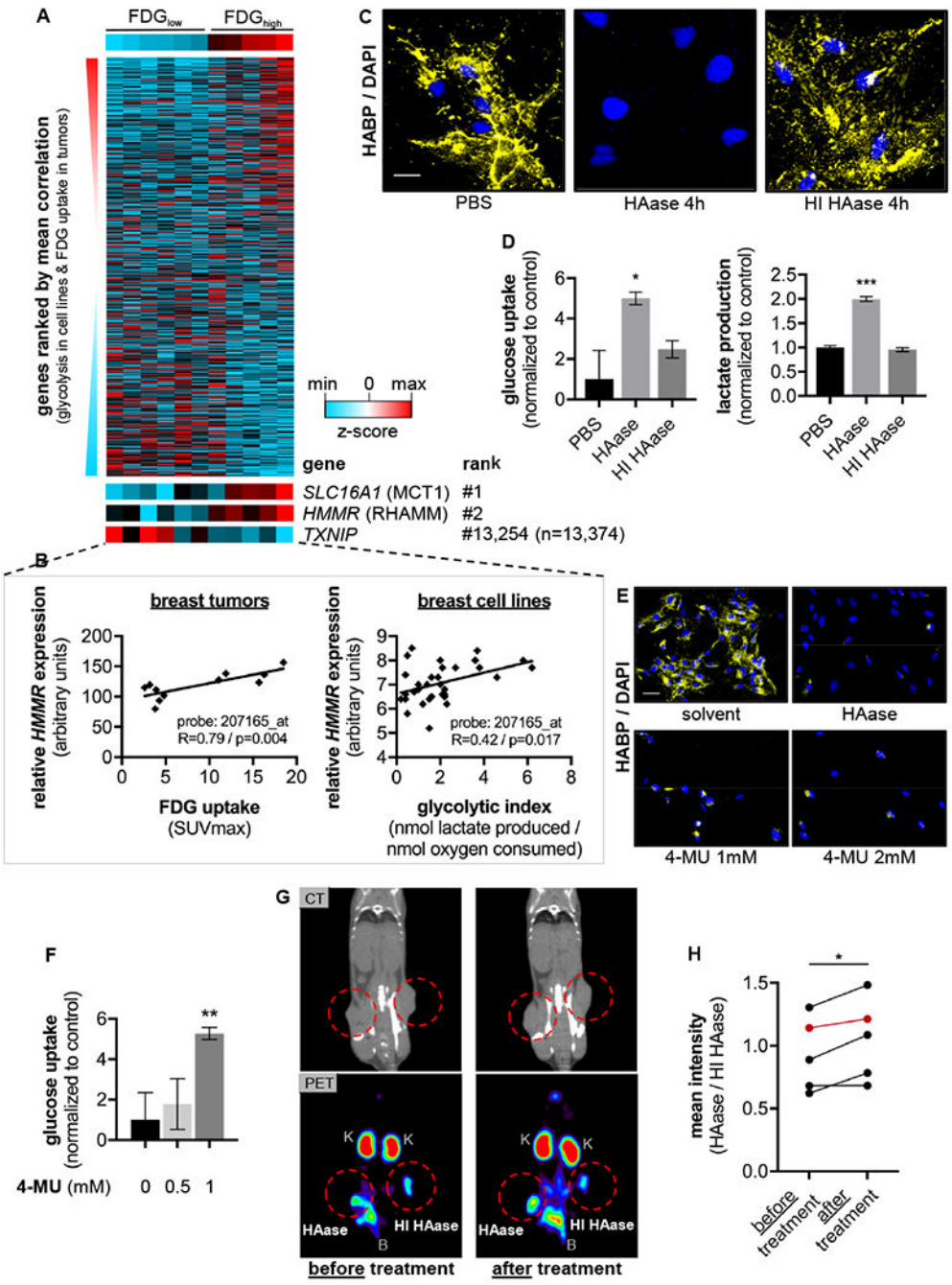

Figure 1: Unbiased analysis identifies ECM engagement as a regulator of glycolytic metabolism.

(A) *(Adapted from* Hong et al., 2016.*)* Genes were ranked on the vertical axis by average correlation of expression with glycolytic index in 31 breast cancer cell lines and with FDG maximum standardized uptake value (SUV_{max}) in 11 patient breast tumors. Tumor transcript levels are presented in order of increasing SUV_{max} on the horizontal axis.**(B)** Linear regressions correlating *HMMR* expression with FDG uptake in patient breast tumors (n=11) and glycolytic index in breast cancer cell lines (n=31). The *HMMR* probe that generated the highest average correlation between tumors and cell lines is shown.**(C)** HABP staining

(yellow) of LiSa-2 cells after treatment with PBS, 400μg/mL HAase, or 400μg/mL heat-inactivated (HI) HAase (concentrations used throughout study unless otherwise stated). Nuclei were stained with DAPI (blue). Scale bar, 25μm.**(D)** Glucose uptake and lactate production rates in LiSa-2 cells treated with PBS, HAase, or HI HAase for 24h. **(E)** HABP staining of LiSa-2 cells treated with 4-MU DMSO 24h prior to fixation. Cells were also treated with PBS or HAase 4h prior to fixation. Scale bar, 50μm.**(F)** Glucose uptake rates in LiSa-2 cells measured between 24h and 48h after treatment with 4-MU DMSO. **(G)** Representative PET and CT images of a SCID mouse bearing A549 xenografts on each flank, at baseline and 6h after intratumoral injection of HAase or HI HAase (indicated by red hatched circle). “K” and “B” indicate kidneys and bladder, respectively. **(H)** Relative tumor FDG signal in each A549 xenografted mouse (n=5 mice), before and after 6h of treatment with HAase and HI HAase. The ratio of mean intensity between the tumor ultimately treated with HAase and that with HI HAase was calculated at baseline and after treatment on a per mouse basis. Ratios for each mouse are displayed. Mouse shown in **(G)** is highlighted in red. All experiments were biological replicates. Error bars denote SD (n=3, unless otherwise indicated). *p<0.05; **p<0.01; ***p< 0.001.

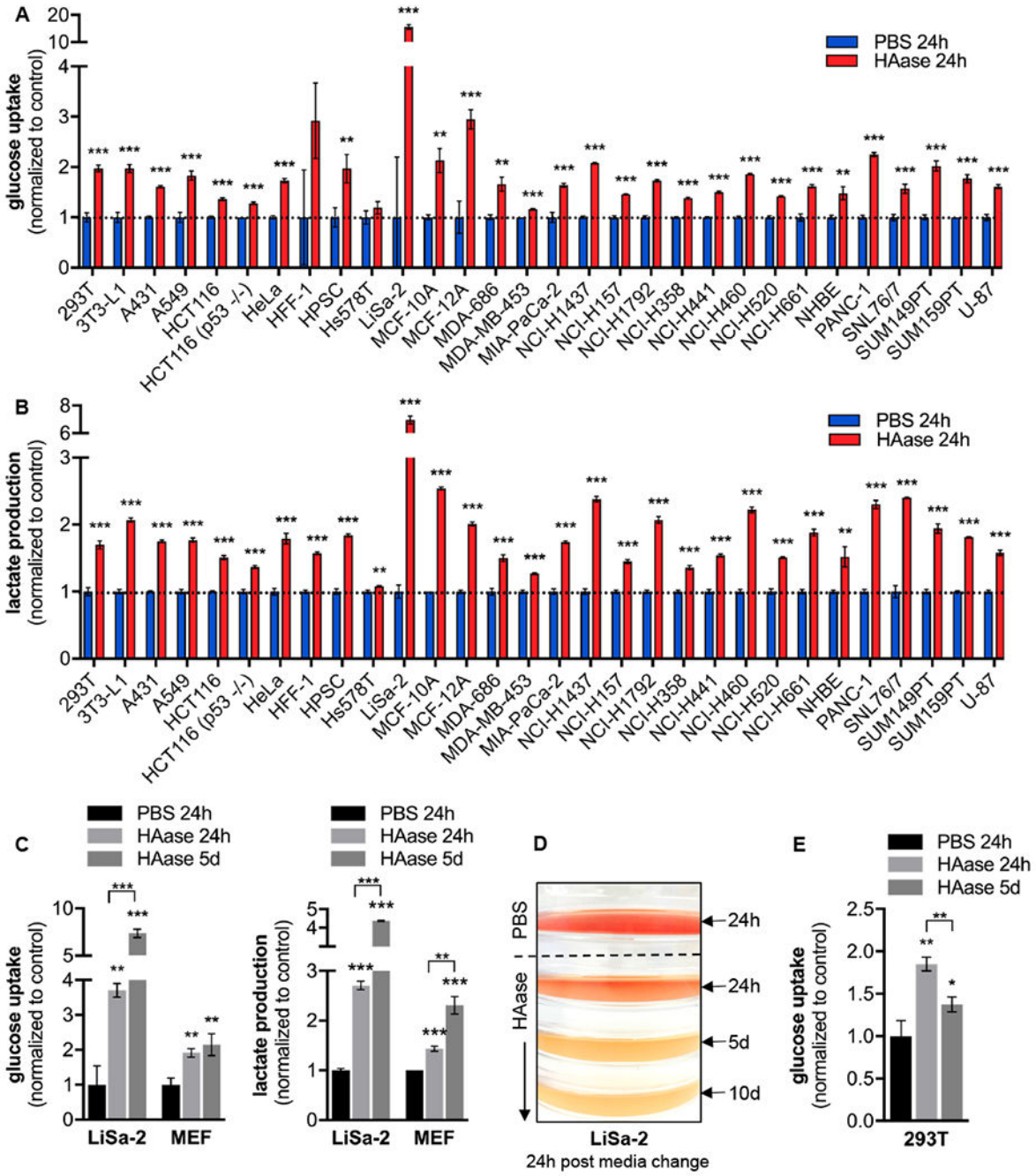

Figure 2: Matrix digestion with HAase acutely increases glycolytic metabolism in a broad range of cultured cells.

(A) Glucose uptake and **(B)** lactate production rates in cultured cells treated with PBS or HAase for 24h. **(C)** Glucose uptake and lactate production rates in LiSa-2 and MEF cells treated with PBS (24h) or HAase (24h and 5d). **(D)** Color change of pH-sensitive phenol red indicative acidification of the culture media. Cells of approximately equal confluency were treated with PBS or HAase for times indicated and incubated in equal volumes of fresh media for 24h. Total cell numbers on each plate ($\times 10^6$): 3.31 PBS, 2.92 HAase 24h, 3.25

HAase 5d, 2.94 HAase 10d. **(E)** Glucose uptake rates in 293T cells treated with PBS (24h) or HAase (24h, 5d). All experiments were biological replicates. Error bars denote SD (n=3). *p<0.05; **p<0.01; ***p< 0.001.

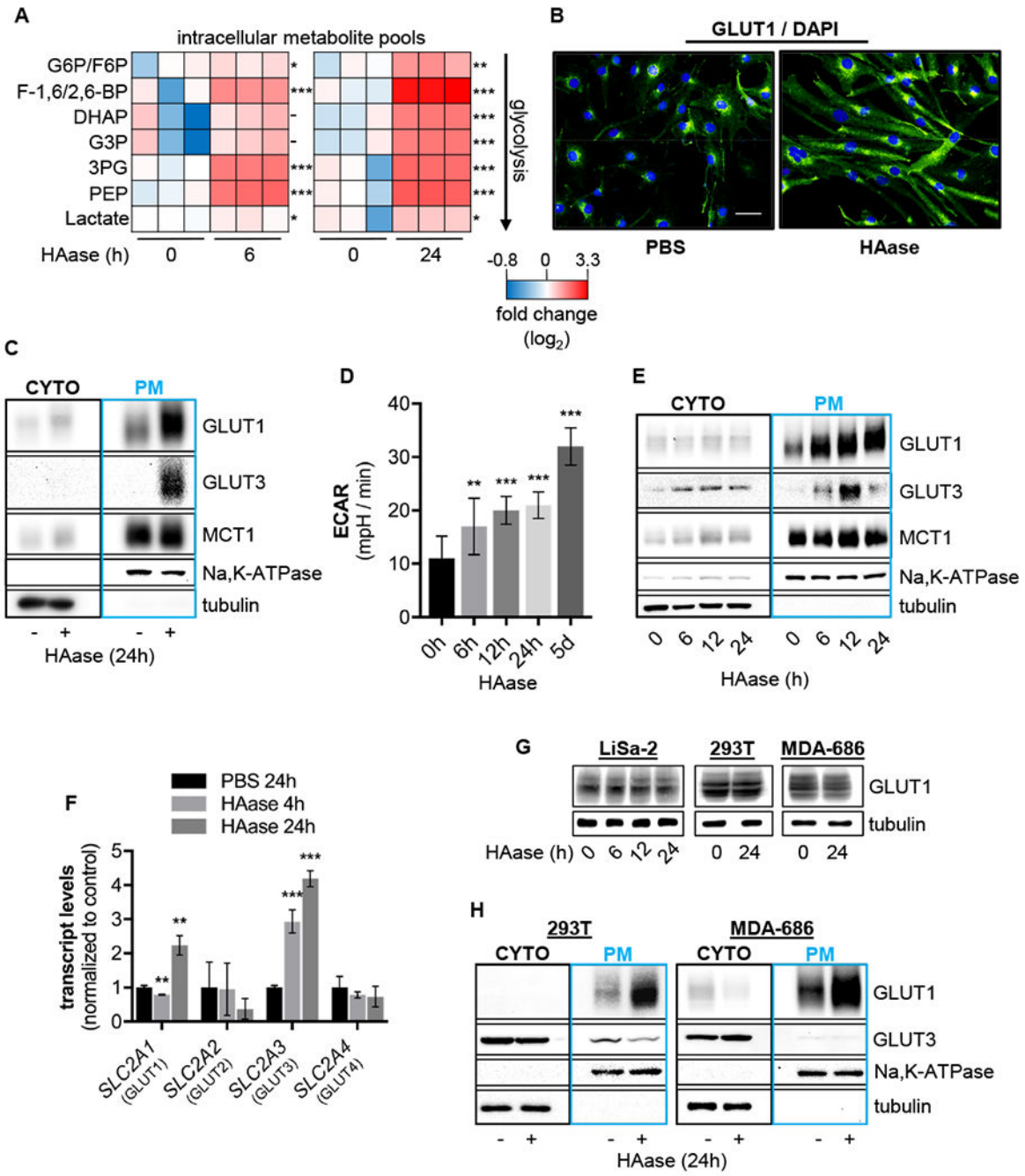

Figure 3: HAase enriches GLUT1 at the plasma membrane.

(A) Heatmaps showing relative intracellular levels of glycolytic intermediates in LiSa-2 cells treated with PBS or HAase. **(B)** Immunofluorescence staining of GLUT1 (green) in LiSa-2 cells following 24h treatment with PBS or HAase. Scale bar, 50μm. **(C)** Immunoblots showing levels of GLUT1, GLUT3, and MCT1 in cytoplasmic (CYTO) and PM fractions of LiSa-2 cells treated with PBS or HAase. **(D)** ECAR of LiSa-2 cells treated with PBS for 24h or HAase for indicated times (n=12 for each condition). **(E)** Immunoblots showing levels of GLUT1, GLUT3, and MCT1 in CYTO and PM fractions of LiSa-2 cells treated with PBS

for 24h or HAase for indicated times. **(F)** Transcript levels of *SLC2A1-4* in LiSa-2 cells following treatment with PBS or HAase. **(G)** Immunoblots showing levels of GLUT1 in whole-cell lysates of LiSa-2, 293T, and MDA-686 cells treated with PBS or HAase. **(H)** Immunoblots showing levels of GLUT1 and GLUT3 in cytoplasmic and PM fractions of 293T and MDA-686 cells treated with PBS or HAase. All experiments were biological replicates. Error bars denote SD (n=3, unless otherwise indicated). **p<0.01; ***p< 0.001.

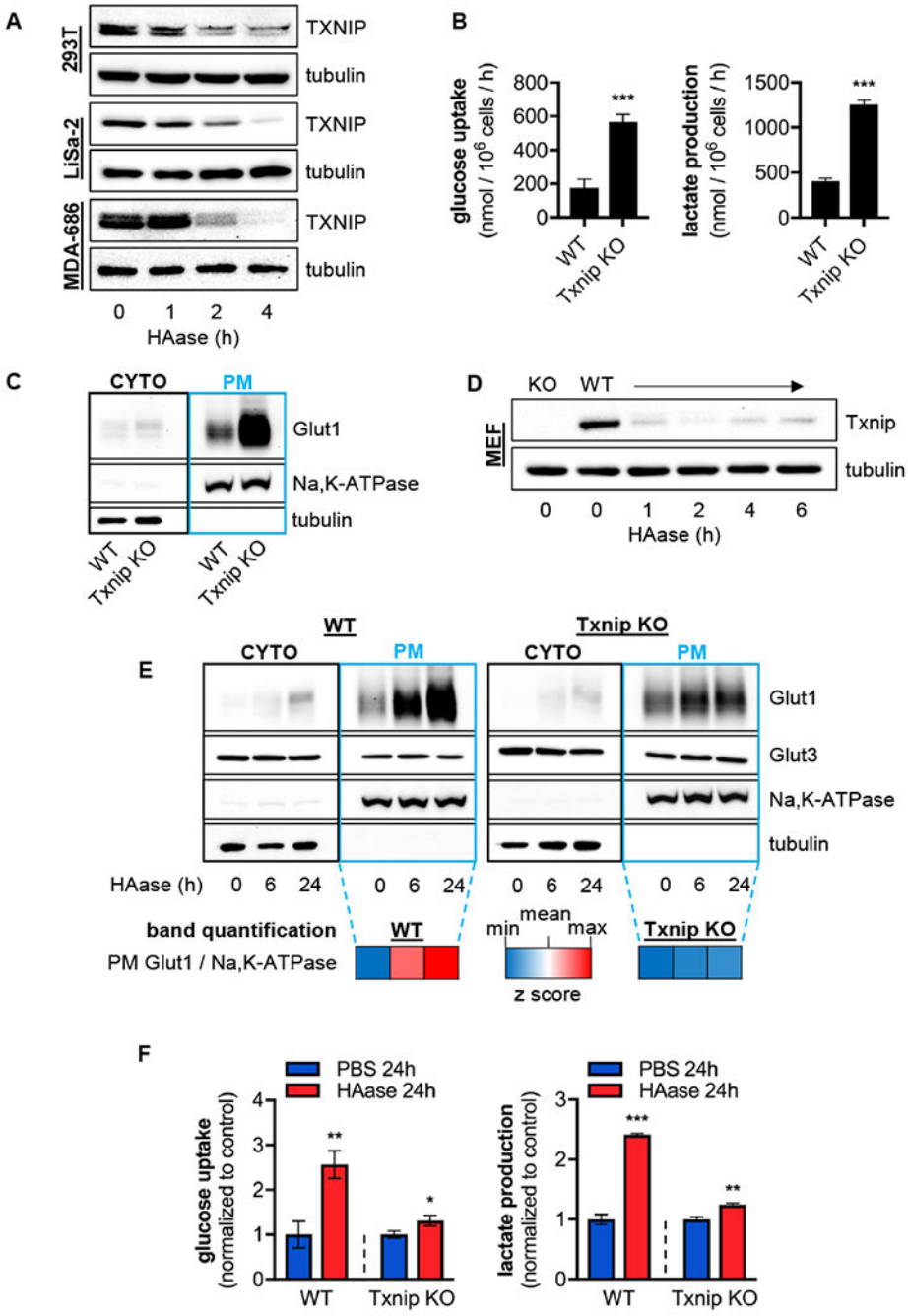

Figure 4: TXNIP reduction largely mediates the acute glycolytic response to HAase.

(A) Immunoblots showing levels of TXNIP in 293T, LiSa-2, and MDA-686 cells treated with PBS (4h) or HAase (1h, 2h, 4h). **(B)** Baseline glucose uptake and lactate production rates in WT and Txnip KO MEFs. **(C)** Immunoblots showing levels of Glut1 in CYTO and PM fractions of WT and Txnip KO MEFs. **(D)** Immunoblots showing levels of Txnip in KO MEFs at baseline and in WT MEFs treated with PBS (6h) or HAase for the indicated times. **(E)** Immunoblots showing levels of Glut1 and Glut3 in CYTO and PM fractions of WT and Txnip KO MEFs treated with PBS (24h) or HAase (6h, 24h). PM Glut1 band intensities

were quantified and normalized to Na,K-ATPase; heatmaps represent z-scores from the resulting ratios. **(F)** Glucose uptake and lactate production rates in WT and Txnip KO MEFs treated with PBS or HAase. Rates for each cell line were normalized to PBS control. All experiments were biological replicates. Error bars denote SD (n=3). *p<0.05; **p<0.01; ***p< 0.001.

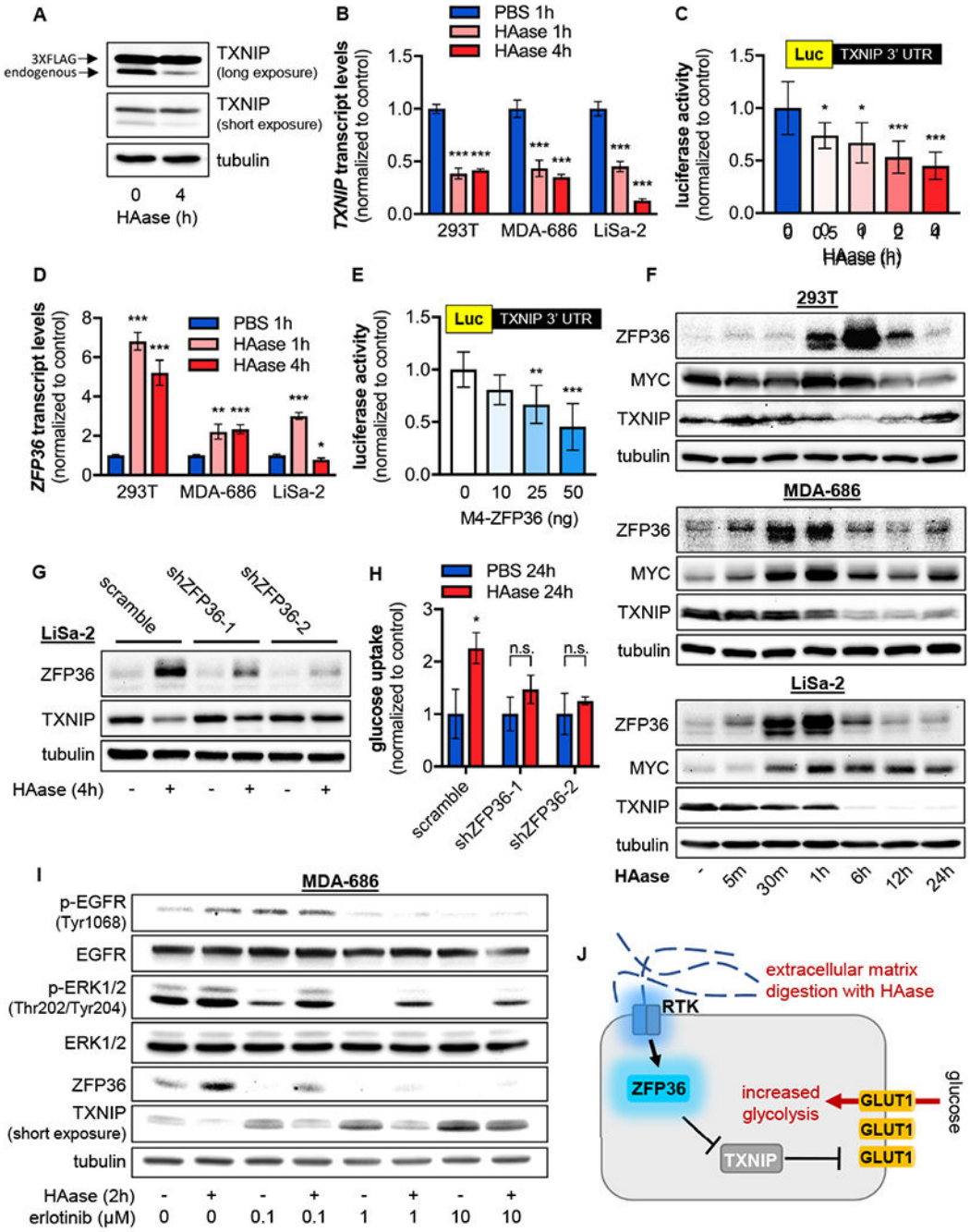

Figure 5: ZFP36 is rapidly induced by HAase and targets *TXNIP* transcripts for degradation.

(A) Immunoblots showing levels of TXNIP in LiSa-2 cells stably expressing a 3xFLAG-tagged version of the protein. Cells were treated with PBS or HAase. **(B)** *TXNIP* transcript levels in 293T, MDA-686, and LiSa-2 cells treated with PBS or HAase. **(C)** Luciferase activity in lysates of HEK293 cells transfected with a *TXNIP* 3' UTR luciferase reporter and treated with HAase (n=6). **(D)** *ZFP36* transcript levels in 293T, MDA-686, and LiSa-2 cells treated with PBS or HAase. **(E)** Luciferase activity in lysates of HEK293 cells co-transfected with a fixed amount of the *TXNIP* 3' UTR luciferase reporter and increasing

amounts of a ZFP36 expression vector (M4-ZFP36)—or the empty vector backbone as a control (n=6). **(F)** Immunoblots showing levels of ZFP36, MYC, and TXNIP in 293T, MDA-686, and LiSa-2 cells treated with a time course of HAase (as indicated), or with PBS (24h). **(G)** Immunoblots showing levels of ZFP36 and TXNIP in LiSa-2 with stable shRNA knockdown of ZFP36 or expression of a scramble control. Cells were treated with PBS or HAase. **(H)** Glucose uptake rates in LiSa-2 cells with stable shRNA knockdown of ZFP36 or expression of a scramble control. Cells were treated with PBS or HAase. **(I)** Immunoblots showing levels of EGFR (Tyr1068 and total), ERK1/2 (Thr202/Tyr204 and total), ZFP36, and TXNIP in MDA-686 cells pretreated for 1h with erlotinib or DMSO control, then with PBS or HAase. **(J)** Proposed model depicting how ECM remodeling promotes acute upregulation of glycolysis. All experiments were biological replicates. Error bars denote SD (n=3, unless otherwise indicated). *p<0.05; **p<0.01; ***p< 0.001; n.s. - not significant.

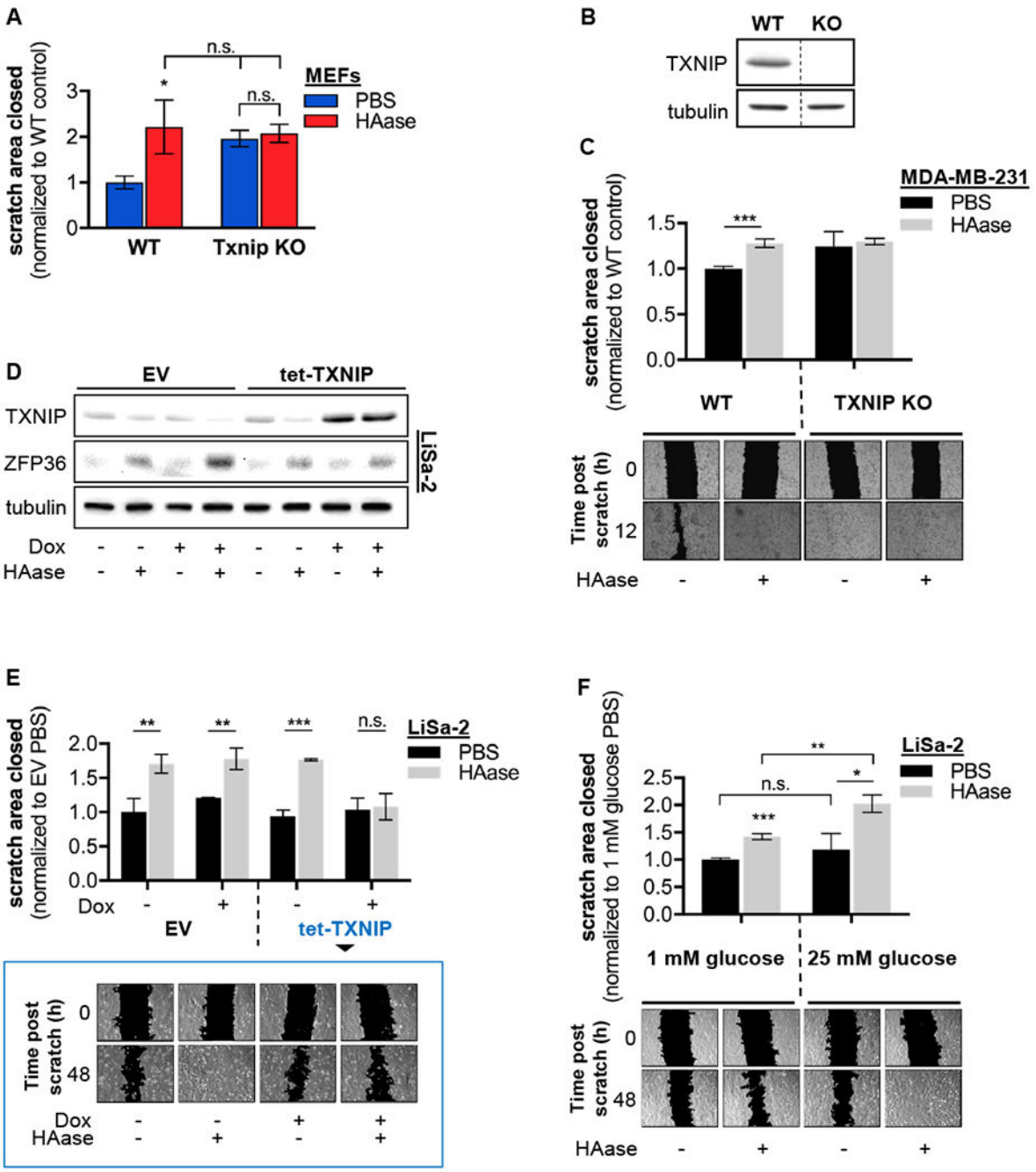

Figure 6: Matrix digestion with HAase accelerates cell migration in a TXNIP- and glucose-dependent fashion.

(A) Scratch assay showing area closed by WT and Txnip KO MEFs after treatment with PBS or HAase for 12h. Representative images are shown in Figure S5D. **(B)** Immunoblots showing levels of TXNIP in WT and TXNIP KO MDA-MB-231 cells. Lanes were cropped from the same membrane, as indicated by dashed line. **(C)** Scratch assay showing area closed by WT and TXNIP KO MDA-MB-231 cells after treatment with PBS or HAase. Representative images are shown. **(D)** Immunoblots showing levels of TXNIP and ZFP36 in

LiSa-2 cells expressing tet-TXNIP (inducible overexpression) or an empty vector control. Cells were pretreated with doxycycline (500ng/mL) or vehicle for 12h, then treated with PBS or HAase for 4h. **(E)** Scratch assay showing area closed by LiSa-2 cells expressing tet-TXNIP or an empty vector control after treatment with PBS or HAase. Cells were pretreated with doxycycline (500ng/mL) or vehicle for 6h. Representative images for tet-TXNIP cells are shown. **(F)** Scratch assay showing area closed by LiSa-2 cells cultured in 1mM or 25mM glucose after treatment with PBS or HAase. Representative images are shown. All experiments were biological replicates. Error bars denote SD (n=3). *p<0.05; **p<0.01; ***p<0.001; n.s. - not significant.

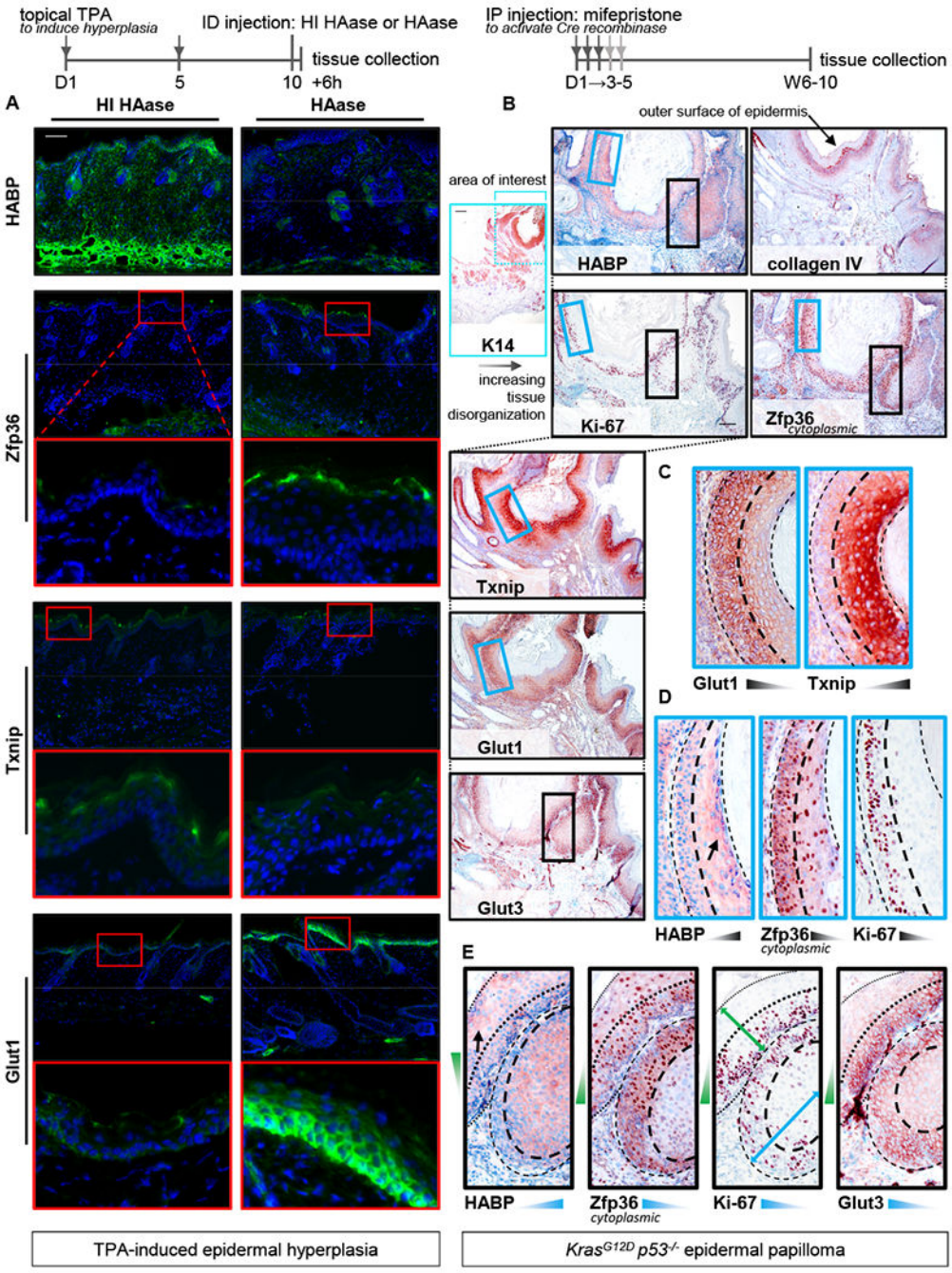

Figure 7: ECM remodeling influences Zfp36-Txnip-Glut1 signaling in tissue.

(A) Immunofluorescence staining of hyperplastic murine epidermis 6h after intradermal injection of HAase or HI HAase. For a given marker, representative images following HAase and HI HAase treatment are from the same animal (opposite flanks; n=4 mice). Red boxes indicate informative regions that are expanded below. Scale bar, 100μm. **(B)** Immunohistochemical staining of an epidermal papilloma (n=5 tumors from 5 mice assessed; 1 shown here). K14 staining distinguishes the epithelial cells within the tissue and demarcates the boundaries of the dermis. Boxes identify comparable architectural reference

points with informative staining patterns; they are expanded in a color-coordinated fashion in **(C-E)** and annotated to demarcate boundaries of tissue structures and to highlight illustrative gradients of signal. Scale bars, 200μm (K14) and 100μm (Ki-67). **(C)** Region highlighting strong anti-correlation between Txnip and Glut1. **(D,E)** Regions highlighting strong HABP anti-correlation with cytoplasmic Zfp36 and Ki-67, as well as Glut3 in **(E)**. Concentrated depositions of HA are indicated by arrows. There are two informative gradients in (E), which are highlighted by blue and green arrows in the Ki-67 panel.